## REPORT DOCUMENTATION PAGE

AFRL-SR-AR-TR-05-

0057



**1. AGENCY USE ONLY** *(Leave blank)*

**2. REPORT DATE**
22 NOV 04

**3. REPORT TYP**
FINAL REPORT 15 JUN 01 TO

**4. TITLE AND SUBTITLE**
RF POLYMER PHASED ARRAY DEMONSTRATION PROJECT

**5. FUNDING NUMBERS**
F49620-01-1-0442

**6. AUTHOR(S)**
PROF. H. FETTERMAN, PROF. W. STEIER, PROF. L. DALTON,
PROF. R. CHEN, AND DR C. COX

**7. PERFORMING ORGANIZATION NAME(S) AND ADDRESS(ES)**
PACIFIC WAVE INDUSTRIES, INC.
10390 SANTA MONICA BOULEVARD, SUITE 100
LOS ANGELES, CA 90025

**8. PERFORMING ORGANIZATION REPORT NUMBER**

**9. SPONSORING/MONITORING AGENCY NAME(S) AND ADDRESS(ES)**
AFOSR/NL
4014 WILSON BLVD., ROOM 713
ARLINGTON, VA 22203-1954

**10. SPONSORING/MONITORING AGENCY REPORT NUMBER**

**11. SUPPLEMENTARY NOTES**

**12a. DISTRIBUTION AVAILABILITY STATEMENT**
APPROVE FOR PUBLIC RELEASE: DISTRIBUTION UNLIMITED

**12b. DISTRIBUTION CODE**

**13. ABSTRACT** *(Maximum 200 words)*

This BMDO demo project was to demonstrate and to evaluate the latest generation of polymer modulators and devices for optical control of phased array radar antennas. Two commercial companies and three universities participated in this effort. Two versions of new phased array antenna designs were demonstrated in Texas on Sept 9, 2004. All of the objectives of the contract were achieved and summarized in this final report. The program involved significant levels of cooperation between the Universities and companies. It really represented a Team effort that brought many different skills and new approaches together. This resulted in several novel directions in designing phased array radars, in combining antennas and modulators, to fabricating new devices and polymer based structures, and to developing new materials for these applications. This report summaries the research in each category by including a write up or major publication. The new devices that were demonstrated permitted rapid control of phased arrays with low cost and weight. They represent a major advance in the State of the Art. However, it is recognized that actual systems that can be implemented devices will require additional investigation to achieve the dynamic range and precise directional control now required for military applications. The domo project showed that electrooptic polymers will play a vital role in future phased array Radar systems. They lend themselves to the complex, integrated systems which will be required in the next generation of combat vehicles and defensive systems. Most important for space based systems they are light and naturally radiation hard.

**14. SUBJECT TERMS**

**15. NUMBER OF PAGES**

**16. PRICE CODE**

| 17. SECURITY CLASSIFICATION OF REPORT | 18. SECURITY CLASSIFICATION OF THIS PAGE | 19. SECURITY CLASSIFICATION OF ABSTRACT | 20. LIMITATION OF ABSTRACT |
|---|---|---|---|

# Final Report for RF Polymer Phased Array Demonstration Project

**2004**

**Pacific Wave Industries**
**UCLA Prof. H. Fetterman**

**University of Southern California**
**Prof. W. Steier, Prof. L. Dalton**

**University of Texas**
**Prof. R. Chen**

**Photonics Systems Inc.**
**Dr. C. Cox**

## Summary

This BMDO demo project was to demonstrate and to evaluate the latest generation of polymer modulators and devices for optical control of phased array radar antennas. Two commercial companies and three universities participated in this effort. Two versions of new phased array antenna designs were demonstrated in Texas on Sept. 9, 2004. All of the objectives of the contract were achieved and are summarized in this Final report. The program involved significant levels of cooperation between the Universities and companies. It really represented a Team effort that brought many different skills and new approaches together. This resulted in several novel directions in designing phased array radars, in combining antennas and modulators, to fabricating new devices and polymer based structures, and to developing new materials for these applications.

This report summaries the research in each category by including a write up or major publication. The new devices that were demonstrated permitted rapid control of phased arrays with low cost and weight. They represent a major advance in the State of the Art. However, it is recognized that actual systems that can be implemented devices will require additional investigation to achieve the dynamic range and precise directional control now required for military applications.

The demo project showed that electrooptic polymers will play a vital role in future phased array Radar systems. They lend themselves to the complex, integrated systems which will be required in the next generation of combat vehicles and defensive systems. Most important for space based systems they are light and naturally radiation hard.

# Index


1. University of Texas System p. 4

2. Pacific Wave's New Chip p. 27

3. University of Southern CA devices p. 34

4. University of Washington & USC Material Development p. 51

5. Photonic Systems Integration of Modulators with Antennas p. 55

## University of Texas X-band PAA demo project

The achievements of the University of Texas Includes the following:

1) A method to achieve continuous-tunable time delay was proposed and developed. The dispersion ability of the holographic-grating true-time delay devices is increased greatly with our approach. The continuous-tunable time delay is achievable by tuning optical wavelength. In addition, we developed a method to record the large diffraction angle in holographic gratings using right-angle prisms.
2) A 4x4 wavelength controlled PAA system was proposed and demonstrated for the first time. The beam steering angles in the elevation and horizontal directions of the developed PAA system are independently controlled by two optical wavelengths. With this system structure, the drawbacks of the current PAA systems, such as physical movement and slow beam steering speed, can be eliminated completely. So high-speed PAA systems can potentially be built with our approach.
3) Analog performance of wavelength conversion using cross-gain modulation in semiconductor optical amplifier are fully characterized and measured for the first time. The wavelength conversion was used to build the 4x4 PAA system. The parameters for analog systems, such as frequency response, 2nd order distortion free dynamic range and noise figure, were measured and analyzed in this demo project.

# Experimental Analysis of Analog Performance of Wavelength Conversion using XGM in SOA for its applications in RF Photonic Systems

Zhong Shi and Ray Chen, Fellow, IEEE

*Microelectronics Research Center, The University of Texas at Austin*
*10100 Burnet Road, PRC/MER 1.606G, Austin, TX 78758*
*Telephone: 512-232-2586, Fax: 512-471-8575, email: raychen@uts.cc.utexas.edu*

**Abstract**: The analog performance of wavelength conversion using cross-gain modulation (XGM) in semiconductor optical amplifier (SOA) has not been fully explored. In this paper, we made extensive experimental analysis of analog performance of wavelength conversion using XGM in SOA. Frequency response, noise figure and distortion free dynamic range are the figure-of-merits for the RF photonic systems. These parameters are investigated in the designed wavelength conversion system within X-band (8-12.5GHz). The analog performance of wavelength conversion using XGM in SOA was optimized in the experiment. The corresponding optimization results are presented in the paper.

## 1. Introduction

Wavelength conversion is a very important technology and has potential applications in all optical networks (AON) to solve the wavelength-blocking problem. Several different schemes for wavelength conversion in SOA have been proposed and demonstrated [1-3]. These research efforts are all made based on the digital signal transmission systems. For the digital signal transmission system, BER is an extremely important parameter to evaluate the performance of the system. However, new applications of wavelength conversion have been also proposed and investigated for the microwave subcarrier multiplexing systems (SCM) [4,5]. In SCM systems, analog format signals are transmitted over the

optical carrier frequencies. In addition, simultaneous transmission of subcarrier multiplexing channels and digital channels is possible in future WDM systems. These analog-signal transmission systems (also called RF photonic systems) are different from the pure digital transmission systems. Analog sinusoidal RF (or microwave) frequency signal is modulated to the optical carrier frequency and then transmitted in the RF photonics systems. The RF (or microwave) signal carried by the optical frequency is converted back into electrical signal at the receiving end of the system. One of the problems for such RF photonics systems is signal distortion. There may be several different optical and electrical components existing within the RF photonic systems, such as optical modulators, EDFAs, SOAs, photo detectors and electrical amplifiers. Any nonlinear transfer function of the above mentioned optical, electrical components or subsystems will generate harmonic or inter-modulation (IM) frequencies which act as distortion to the original signal. The generation of distortion frequencies will decrease the signal power and degrade system performance eventually. Distortion free dynamic range is usually used to characterize the ability of the system to suppress the distortion generation. Beside the distortion free dynamic range, frequency response and noise figure (NF) are the other important figure-of-merits of the RF photonic system. Reference [5] investigated the frequency response performance of wavelength conversion using cross-gain modulation in SOA. However, to fully characterize the analog performance of wavelength conversion, noise figure and distortion free dynamic range need to be measured and optimized. In this paper, extensive experimental results of wavelength conversion using XGM in SOA are presented for its applications in the RF photonic systems. The figure-of-merits of wavelength conversion within microwave X-band (8-12.5GHz) was measured and optimized. The optimization results are reported in the paper.

## II. Experimental Setup

The experimental setup for wavelength conversion is shown in Fig. 1. The counter-propagation structure was used instead of the co-propagation structure to avoid using optical filter at the output end of SOA. The pump external-cavity laser (ECL) having a wavelength of 1551nm ( $?_1$ ) was modulated by a standard $LiNbO_3$ Mach-Zehnder intensity modulator. An HP network analyzer (8510C) was used to provide a purely sinusoidal electrical signal to the modulator. The modulated optical signal was amplified by an Er-doped fiber amplifier (EDFA) as the modulator has ~8dB loss. A variable optical attenuator (VOA) was right after EDFA to adjust the input pump optical power for the system optimization purpose. The output of VOA was coupled to SOA through a 1x2 optical coupler. The probe ECL having a wavelength of 1542nm ( $?_2$ ) was coupled into SOA from the other end. The signal carried by $?_1$ was transferred to $?_2$ through XGM effect within SOA cavity. After wavelength conversion, the signal carried by $?_2$ was coupled out from the 1x2 coupler and then converted back to electrical domain by a PIN photodetector. The electrical signal was analyzed by an HP microwave spectrum analyser (MSA).

For the counter-propagation structure based wavelength conversion, the wavelength of the microwave signal should be much bigger than the SOA cavity length to avoid the signal cross-interference effect between the two directions [6]. Otherwise, the conversion signal will be scrambled at the output end of SOA. In our experiment, the interested microwave frequency range is from 8GHz to 12GHz that is in the microwave X-band. The corresponding wavelength is from 3.75cm to 2.5cm that is much larger than the cavity length (~700 $?m$). So the signal cross-interference effect is negligible in the experiment.

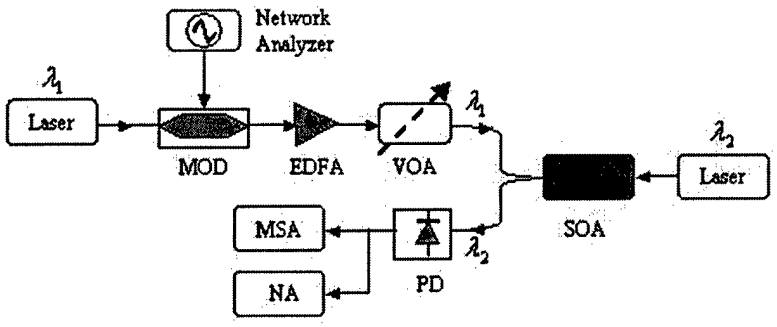


Fig. 1: Experimental setup for counter-propagation based wavelength conversion.

MOD: modulator, EDFA: Er-doped fiber amplifier, VOA: variable optical attenuator, SOA: semiconductor optical amplifier, PD: photo detector MSA: microwave spectrum analyser, NA: network analyzer

## III. Experimental results

(1)Link gain optimization

The first step of our experiment is to optimize the output electrical signal from the photodetector. Link gain is sometimes used to characterize the electrical signal conversion efficiency of the RF photonic systems [7]. It is defined as the ratio of the output electrical signal power from the photodetector to the input electrical signal power to the optical modulator. The link gain can be expressed in dB as:

$$G ? 10\log(\frac{P_{e,out}}{P_{e,in}})$$

(1)

where $P_{e,out}$ is the output electrical power from the photodetector, $P_{e,in}$ is the input electrical power to the optical modulator. In our experiment, the input electrical power to the optical modulator $P_{e,in}$ was kept constant. We only need to optimize the output electrical power $P_{e,out}$ from the photodetector to get an optimum link gain. The input optical pump power and the bias current of SOA are important factors in determining

the gain saturation of SOA. The gain saturation of SOA will determine the output electrical power from the photodetector. So we measured the output electrical power at the different input optical pump powers and bias currents of SOA. Fig. 2 is the measurement results of the output electrical power vs. input optical pump power at 140mA bias current. The results shown in Fig. 2 are normalized by the peak value at 8GHz. The input optical probe power was kept constant at -1dBm. Three different frequencies were measured in the experiment: 8GHz, 10GHz, and 12GHz, which all lie within the microwave X-band. From the measurements we can see that the transfer curves of the wavelength conversion at the three different frequencies behave very similarly. The output electrical power increases gradually and shows very good linearity before reaching the peak value. Beyond the peak value, the curves appear roll-off phenomenon that is due to the gain saturation of SOA. The maximum output electrical power was achieved when the input pump optical power is 0~1dBm for the three frequencies. The curve roll-off can be further explained by gain curve measurements shown in Fig. 3. It is easy to see that gain of SOA is approaching zero when the input optical power is larger than 0dBm. At this small gain region, most of the carriers within the cavity are consumed by the input optical pump power. The conversion signal gets less and less gain with increasing input optical pump power, which leads to the roll-off of the curves. The transfer curves in Fig. 2 are measured for XGM based wavelength conversion in SOA. Similar measurement results were also found for XPM based wavelength conversion in nonlinear fibers [8]. Fig. 4 shows the normalized output electrical power from photodetector when the bias current was changed from 85mA to 170mA. We measured at the three different frequencies: 8GHz, 10GHz and 12GHz. For each curve, we can see that the output electrical power is directly proportional to the bias current of SOA. The saturation appears when the bias current exceeds 140mA. According to this measurement increasing bias current helps to

increase the output electrical power (link gain). However, SOA will generate a lot of heat and the stability of SOA will become a problem at the high bias current. In the following experiment, the bias current of SOA was kept at 140mA as we found SOA worked very well at this bias current.

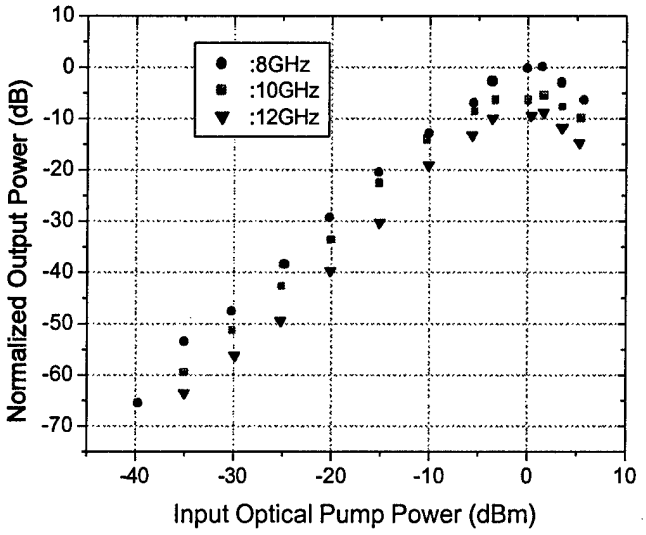


Fig. 2: Output electrical power (link gain) optimization measurement.

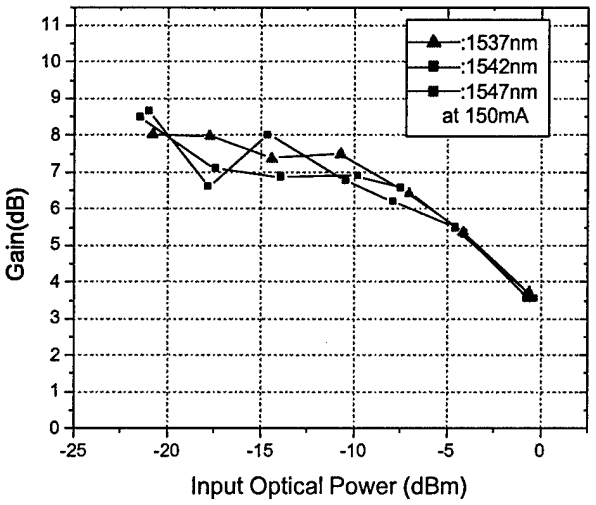

Fig. 3: Gain vs. input optical power measurement.

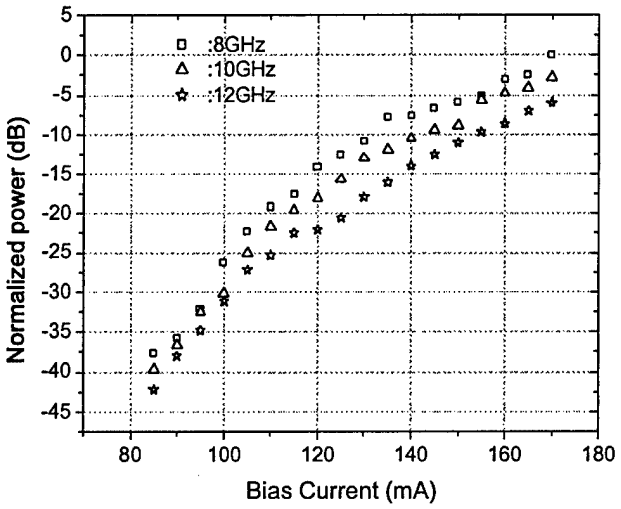


Fig. 4 Electrical output power vs. bias current of SOA

(2) Frequency response measurement

Frequency response is an important parameter which is usually used to determine the bandwidth of a given device or system. To measure the frequency response of the wavelength conversion, an HP network analyzer (8510C) was used to analyze the electrical signal from photodetector. Only one microwave frequency was provided to the optical modulator in the measurement. Fig. 5(a) and (b) are the measured frequency response for the fundamental frequency and its second harmonic frequency. The second harmonic frequency serves as distortion component within the system. The measurement of the fundamental frequency was made from 200MHz to 12GHz. The corresponding second harmonic frequency was measured from 400MHz to 24GHz. From 200MHz to 12GHz, the frequency response of the fundamental frequency drops about 9dB. For our interested X-band frequency region, the response of the fundamental frequency decreases about 3dB. Fig. 5(b) shows the frequency response of the second harmonic frequency. The response of the second harmonic frequency drops about 32dB when the

fundamental frequency is changed from 200MHz to 12GHz. The frequency response of the fundamental frequency drops much slower than that of its second harmonic frequency within the wavelength conversion system, especially at high frequency region as indicated. Fig. 6 shows the power difference between the fundamental frequency signal and the corresponding second harmonic frequency. At the zero reference point (fundamental frequency: 200MHz), the power difference is 15dB between the fundamental frequency signal and its second harmonic frequency. A more than 30dB power difference exists between the fundamental frequency and its second harmonic frequency within the X-band, i.e. 8 to 12.5GHz.

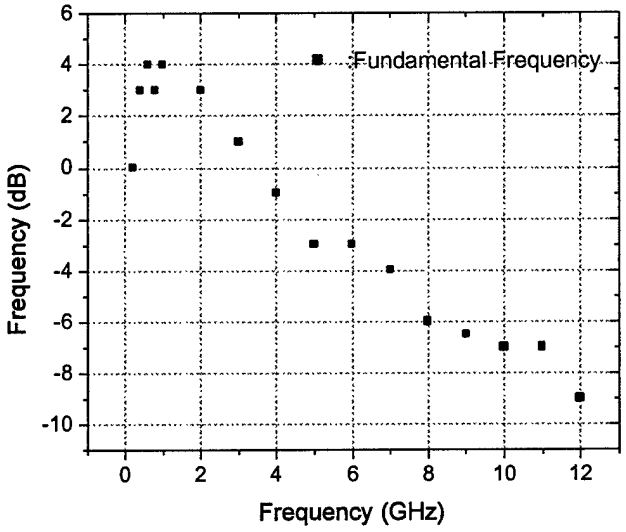


Fig. 5(a) Frequency response measurement for fundamental frequency

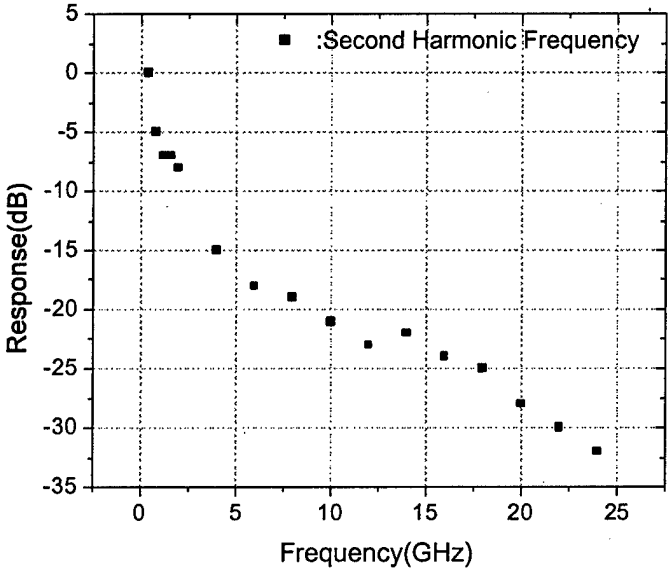


Fig. 5(b) Frequency response for second harmonic frequency.

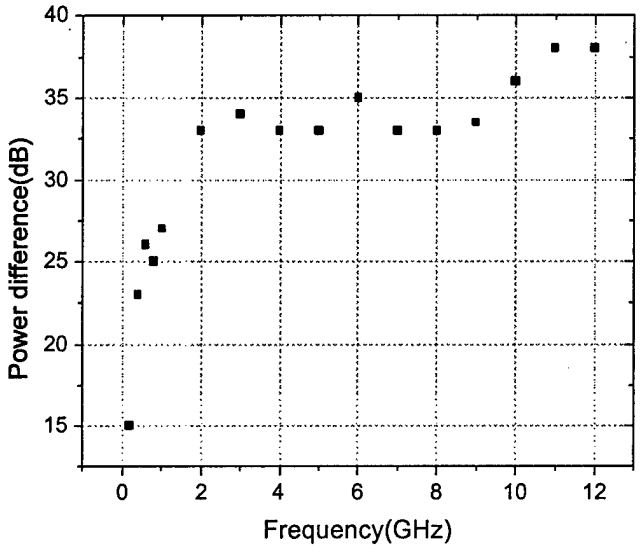


Fig. 6. Power difference between the fundamental frequency and the corresponding second harmonic frequency.

(3)Noise figure measurement

Noise figure (NF) is an extremely important parameter to be measured for a RF photonic system. It describes how much noise has been added to the original signal within a system. Its general definition is the ratio between the input signal-to-noise ratio and the output signal-to-noise ratio. Following the similar steps in [9], we can get the following NF equation for wavelength conversion using XGM in SOA:

$$NF \; ? \; \frac{(SNR)_{in}}{(SNR)_{out}} \; ? \; (\frac{m_1^2 P_1 v_2}{m_2^2 P_2 v_1})[2(1 \; ? \; \frac{1}{G})n_{sp} \; ? \; \frac{1}{G}] \quad (2)$$

where $(SNR)_{in}$ and $(SNR)_{out}$ are input signal-to-noise ratio and output signal-to-noise ratio, respectively. $m_1$ and $m_2$ are the modulation depth for $?_1$ and $?_2$, respectively. $P_1$ is the input optical power to SOA for $?_1$. $P_2$ is the output optical power from SOA for $?_2$. $?_1$ and $?_2$ are the corresponding frequencies of $?_1$ and $?_2$, respectively. $n_{sp}$ is spontaneous emission factor. Equation (2) is similar to that derived for EDFA in [9], but we need to consider different AC signal power carried by the two wavelengths. From equation (2), we can see gain $G$ of SOA and AC signal power carried by the two wavelengths will determine NF. The gain of SOA and AC signal power carried by the two wavelengths are primarily determined by the bias current of SOA and the input optical pump power. So we measured NF at different bias current of SOA and input optical pump power. Fig. 7(a) is the measured NF vs. bias current of SOA. NF is almost linearly proportional to the bias current according to the measurement of Fig. 7(a). The measured NF is considerably improved from 34dB to 14.5dB when the bias current is increased from 80mA to 180mA. In measuring Fig. 7(a), the input optical pump power is kept at 0.5dBm and the wavelength is 1551nm ( $?_1$ in Fig. 1). The input optical probe power is -1dBm and the wavelength is 1542nm ( $?_2$ in Fig. 2). Fig.

7(b) shows the measured NF at different input optical pump power. We found that NF is inversely proportional to the input optical pump power. This is actually due to the gain saturation effect. Although decreasing input optical pump power helps to increase NF, it will decrease output electrical power at the same time which can be seen from the measurements in Fig. 2. As a result, there is a tradeoff in optimizing output electrical power and NF. As mentioned before, when the input pump optical power is 0~1dBm, we achieved the optimized output electrical power from photodetector. We are going to show in the next part that distortion free dynamic range will also benefit from increasing input optical pump power. Considering this, in the experiment we still maintained the input optical pump power at 0~1dBm and the input optical probe power at -1dBm which corresponds a NF of ~18.5dB at 140mA bias current according to the measurement results in Fig. 7(b).

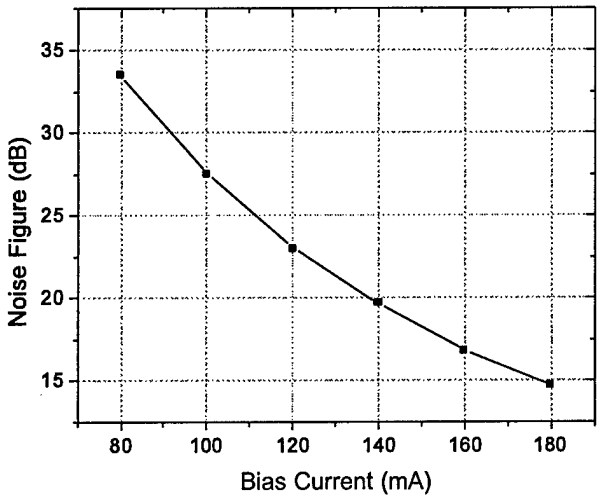


Figure 7(a) Noise figure measurement under different bias current and

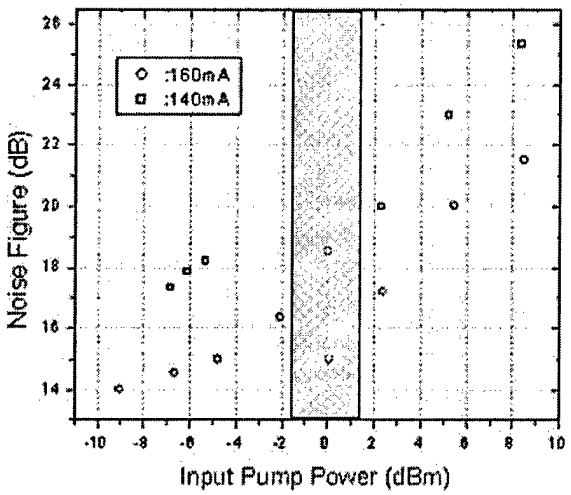


Fig. 7(b) Noise figure measurement under different input pump power.

(4)Second harmonic distortion free dynamic range measurement

Before we measured the distortion free dynamic range (DFDR), we optimized the bias voltage of the optical modulator. This is important because any harmonic freqeuncies generated in the modulation will decrease the analog modulation modulation efficiency of the optical modulator, and, further decrease the wavelength conversion efficiency also. Fig. 8 is the setup used for optimizing the bias voltage of the optical modulator. The modulator modulated the incoming light from an ECL laser and the microwave signal came from the HP network analyzer. After modulation a VOA was used to adjust the input optical power to the photodetector to prevent its saturation at high optical input power. The HP MSA was used to receive and analyze the output power from the photodetector. To make the measurement, the bias voltage of the modulator was changed from 0.04V to 5.1V. The output optical power from modulator was measured first using an optical spectrum analyzer (OSA). The measurement results are shown with the black dots in Fig. 9.

This is actually the transfer curve of the modulator. From the measurement it can be seen that the modulator has a $V_\pi$ ~3V. Then the electrical power from the photodetector was measured for both the fundamental frequency and the second harmonic frequency using MSA at the microwave modulation frequency 8GHz. The power difference (2HD) between the fundamental frequency and the second harmonic frequency is also shown in Fig. 9 with the white dots. We can see that the 2HD is optimized when the bias voltage is at 0V or 4.4V. From the transfer curve in Fig. 9 we can see that these two points actually work in the linear modulation region of the modulator. The smallest 2HD is –34dBc at a bias voltage of 4.4V. So in the experiment, 4.4V bias voltage was used to minimize the harmonic generation within the system. One thing needs to be noticed is that asymmetry curve of 2HD measurement. We believe the DC operation drifting of the modulator and the different response of photodetector to the different input optical power are the two sources leading to the asymmetry of 2HD measurement.

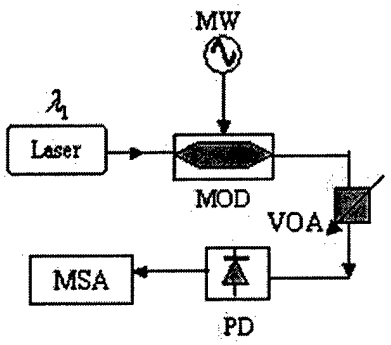


Fig. 8 Setup for optimizing DC bias point of the modulator

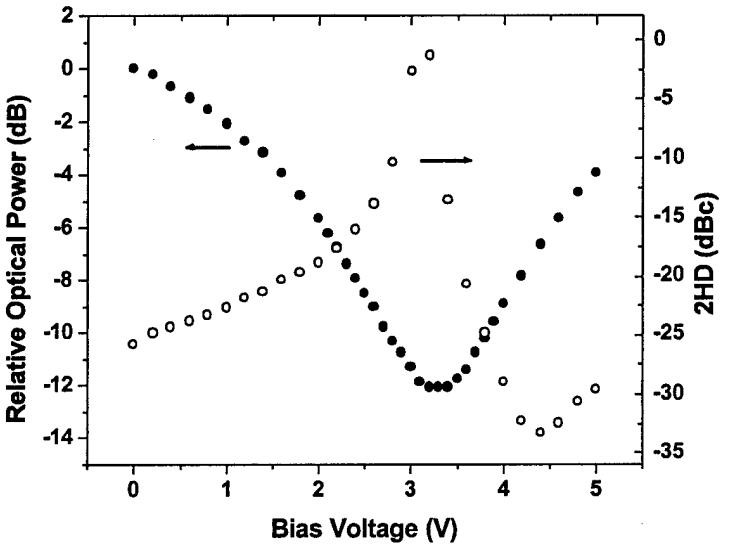


Fig. 9. Modulator bias point optimization measurement

After modulator was optimized, we measured the distortion free dynamic range of the designed system (DFDR). DFDR is an important parameter needed to be characterized for RF photonics system. Spurious-free dynamic range (SFDR) is important for a two-tone input system. This is because the generated third order inter-modulation (IM) frequencies ( $2f_1 ? f_2$ or $2f_2 ? f_1$ ) are the closest to the fundamental frequencies and very difficult to be filtered out. They will serve as noise to the desired signals after optical-to-electrical conversion. Second harmonic distortion free dynamic range is important for a multi-tone inputs system as the generated harmonic frequencies ( $f_2 ? f_1$ , $f_2 ? f_1$ , $2f_2$ , $2f_1$ ) can potentially be noise sources to signal frequencies within the system. According to our measurement, the power of third-order IM frequences ($2f_1 ? f_2$, $2f_2 ? f_1$) is very close to noise level (-130dBm @100Hz) with the available input electrical power in our system. However, from the frequency response measurement shown in

Fig. 5(b) and Fig. 6 we found considerable second harmonic frequency generated in the system. So we focused on the measurement of the second harmonic distortion free dynamic range. Since only one microwave frequency $f$ was used, we need to consider $2f$ only in the measurements.

Fig. 10(a) is the measured output electrical power for the fundamental frequency and the second harmonic frequency versus the input electrical power to the optical modulator. As expected, the fundamental frequency term and the second harmonic frequency term have slopes of 1 and 2 respectively. In the experiment the noise floor is about −130dBm. The linear curves are extrapolated to intersect the noise floor. Then the second harmonic distortion free dynamic range can be derived from the power difference at the two intersection points between the fundamental frequency and the second harmonic frequency. The corresponding measurement results are shown in Fig. 10(b). In the experiment we first measured the second harmonic distortion free dynamic range before wavelength conversion. This is actually a measurement of optical modulator itself. The measured result is about 50.6dB-$Hz^{1/2}$ and this value is not sensitive to the input optical power. Then the second harmonic distortion free dynamic range was measured after wavelength conversion. The measurement was made at different input optical pump power: -5.88dBm, -1.93dBm and 0.43dBm. The corresponding second harmonic distortion free dynamic range was 45.6dB-$Hz^{1/2}$, 48.7dB-$Hz^{1/2}$, and 53.7dB-$Hz^{1/2}$. From this measurement it's easy to see that increasing the input pump optical power helps to increase the second harmonic distortion free dynamic range, which is actually due to the increase of the wavelength conversion efficiency that is observed already in Fig. 2. We could expect the decrease of the second harmonic distortion free dynamic range once the input optical pump power exceed the 2dBm which will cause the gain over-saturation of SOA and decrease of

wavelength conversion efficiency. To further verify the above results, we make the same measurements but using a different microwave frequency: 12GHz. The Fig. 11(a) shows the measurement results for both the fundamental frequency and the second harmonic frequency. We measured the second harmonic distortion free dynamic range for modulator at 12GHz first and it was determined to be 56.75dB-$Hz^{1/2}$. We also made the measurement after wavelength conversion with different input optical pump power for the fundamental frequency at 12GHz. The corresponding results are shown in Fig. 11(b). The measured second harmonic distortion free dynamic ranges are 48.75dB-$Hz^{1/2}$ and 52.5dB-$Hz^{1/2}$, respectively, for the input optical pump power at −1.93dBm and 0.43dBm. The second harmonic distortion free dynamic range will increase when increasing input optical pump power in Fig. 11(b), which agrees with the measurement results in Fig. 10(b). One interesting thing needs to be pointed out is that the second harmonic distortion free dynamic range for the optical modulator at 12GHz is about 56.75dB-$Hz^{1/2}$ which is higher than that measured at 8GHz. This result seems not reasonable. Actually this is not surprising as it can be explained from the frequency response measurement of the optical modulator. The frequency response of the modulator is shown in Figs. 12(a) and 12(b). Fig. 12(a) is made for the fundamental frequency and Fig. 12(b) is for the second harmonic frequency. Fig. 13 shows the power difference between the fundamental frequency and the second harmonic frequency measured when the fundamental frequency was swept from 200MHz to 12GHz. The frequency response difference at 12GHz is about 42dB which is larger than that with a 36dB at 8GHz. This larger frequency response difference at high frequency makes the distance between the two intersection points at the noise level in Fig. 11(a) is larger than that in Fig. 10(a) for the modulator measurement. However, for the second harmonic distortion free dynamic range measurement after wavelength conversion, we didn't find an obvious difference between 8GHz and

12GHz since there is only a 3dB response dropping across the X-band. To keep the designed system operating with a high second harmonic distortion free dynamic range, we have to keep the input optical pump power in 0~1dBm. However, as stated above, any further increase of this input optical pump power may decrease the second harmonic distortion free dynamic range due to the decrease of the output electrical power from the photodetector due to the gain over-saturation of SOA.

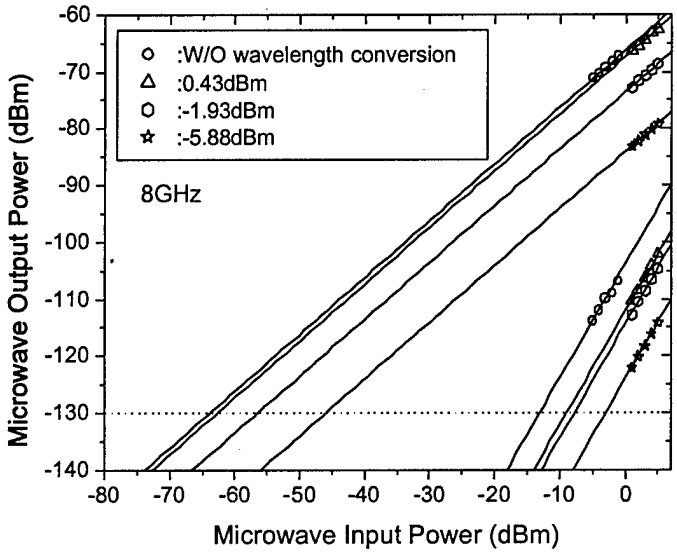


Fig. 10(a) Second harmonic distortion free dynamic range measurement at 8GHz

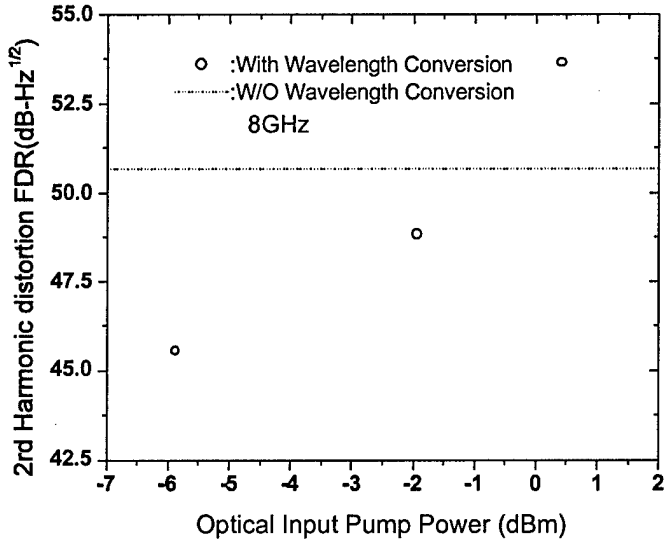


Fig. 10(b) Second harmonic distortion free dynamic range measurement at 8GHz

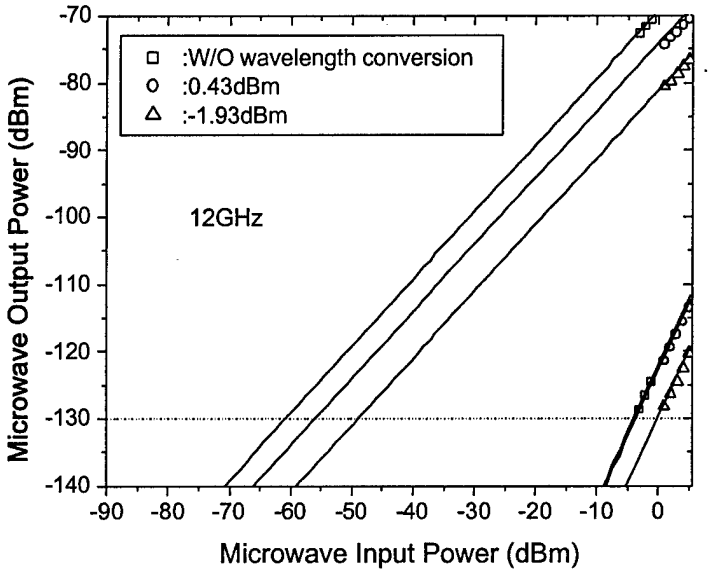


Fig. 11(a) Second harmonic distortion free dynamic range measurement at 12GHz

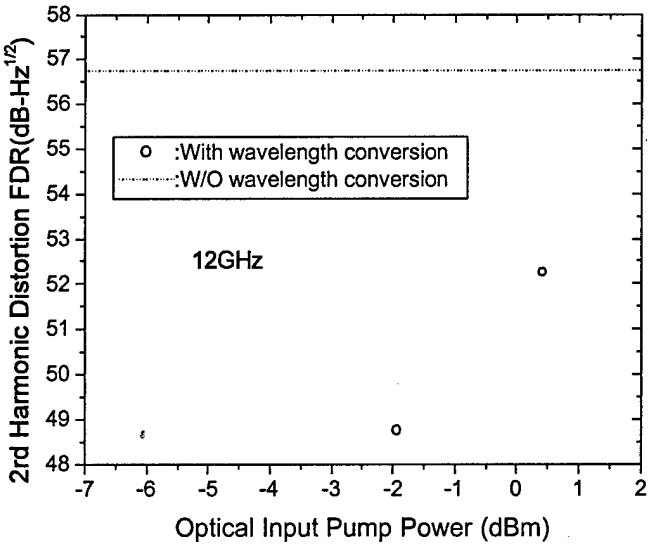


Fig. 11(b) Second harmonic distortion free dynamic range measurement at 12GHz

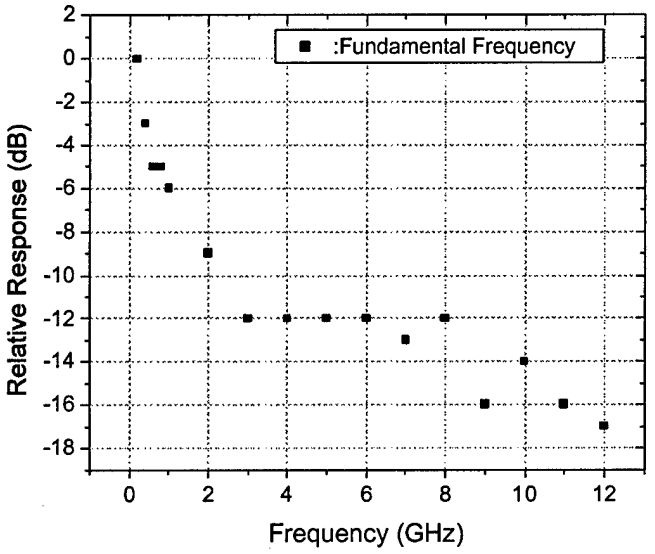


Fig. 12(a) Response measurement of optical modulator for the fundamental frequency

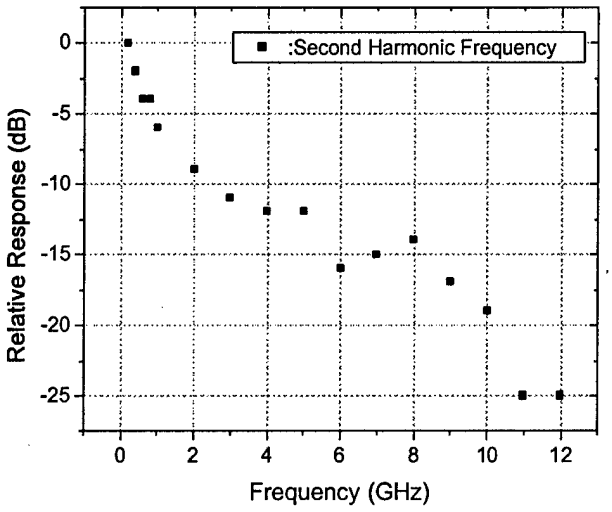


Fig. 12(b) Response measurement of optical modulator for the second harmonic frequency

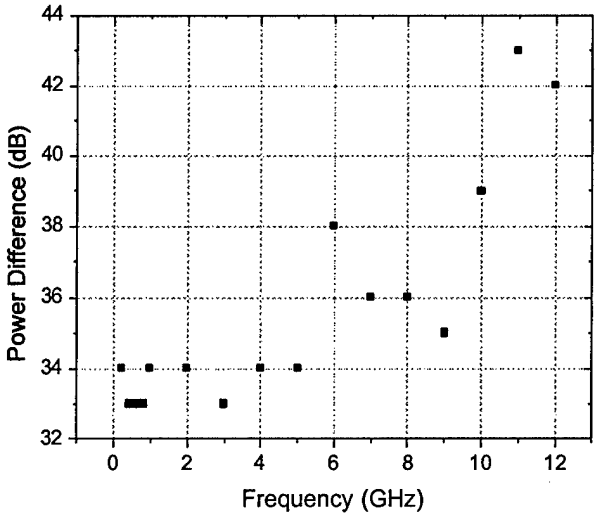


Fig. 13. Power difference between the fundamental frequency and the corresponding second harmonic frequency

## IV Conclusion

Extensive experimental analysis of analog performance of wavelength conversion using XGM in SOA is reported in this paper. The output electrical power (link gain) was optimized first with respect to the input optical pump power and the bias current of SOA. The response of the fundamental frequency and the second harmonic frequency of the designed system was also measured. The response of the fundamental frequency was measured up to 12GHz. The noise figure was measured for different bias current and input optical pump power. Considering the overall system optimization, we determined the NF to be 18.5dB for the designed system. Furthermore, we also measured the second harmonic distortion free dynamic range at 8GHz and 12GHz. We found increasing the input optical pump power to a certain level will help to increase the second harmonic distortion free dynamic range. We determined the input optical pump at 0~1dBm will optimize the performance of the designed system.

## References


1 K. E. Stubkjaer, Semiconductor amplifier-based all optical gates for high-speed processing, IEEE J. Select. Topics Quantum Electron., Vol. 6, pp. 1428-1435, Nov./Dec. 2000

2 T. Durhuus, C. Joergensen, B. Mikkelsen, R. J. S. Pedersen, and Ke. E. Stubkjaer, All optical wavelength conversion by SOA's in a Mach-Zehnder configuration, IEEE Photonics Technology Letter, Vol. 6, pp. 53-55, January 1994

3 M. C. Tatham, 20nm optical wavelength conversion using nondegenerate four wave mixing, IEEE Photonics Technology Letter, Vo. 5, 1303-1305, Nov. 1993.

4 W. Shieh, E. Park, and A. E. Willner, All-optical wavelength shifting of microwave subcarriers by using four-wave mixing in a semiconductor optical amplifier, IEEE Photonics Technology Letter, Vol. 8, No. 4, April, 1996.

**5** Jose Capmany, Salvador Sales, Daniel Pastor, Alfonso Martinez, and Beatriz Ortega, Wavelength conversion of SCM signals using semiconductor optical amplifiers: theory, experiments, and applications, IEEE J. of Lightwave Technol., Vol. 21, pp. 961-972, April 2003.

6 Jesper Mork, Mads L. Nielsen and Tommy W. Berg, The dynamics of semiconductor optical amplifiers: modelling and applications, Optics & Photonics News, 43, pp. 42-48, July 2003

7 W. S. C. Chang, RF photonic technology in optical fiber links, Cambridge, 2002

8 Lavanya Rau, Roopesh Doshi, Suresh Rangarajan, Yijen Chiu, D. J. Blumenthal, and Je. E. Bowers, Analog performance of an ultrafast sampled-time all-optical fiber XPM wavelength converter, IEEE Photonics Technology Letter, Vol. 15, pp. 560-562, April 2003.

9 Emmanuel Desurvire, Erbium-Doped Fiber Amplifiers: Principles and Applications, John Wiley & Sons, Inc., 1994.

## Pacific Wave

The Demo Project from Pacific Wave with support from UCLA involved the development of an optically controlled Phase Shifter that was configured to rapidly tune four elements on a single integrated chip. The system was then configured to use four of these chips to make a four by four array. New MMI elements and on chip optical crossing were developed in this project. In addition, a unique balancing arm was introduced to cancel the carrier, in the single sideband modulator element, and to improve the linearity of the device.

The device was tested with the new structure with balancing arm and was found to have a much wider angular directional capability because of this modification. The variation in the amplitude of the signal was also significantly reduced making this a much more useful antenna controller.

In addition to this polymer phased array phase shifter a new type of DOS polymer switch was developed for true time implementations. This is expected to have important applications in the next generation of devices.

# Photonic RF Phase Shifter for Electrooptic Polymer Optically Controlled Beam Forming Systems

Phased array antenna beam forming systems have become increasingly important in advanced wireless communications such as mobile radio communications, wireless local area networks (LANs) and satellite communications as well as radars. In contrast to dish or slotted array antennas, which use either physical shape or direction to form and steer beams, phased array antennas provide highly directional far-field lobe patterns by utilizing the interference of the fields emitted from a large number of regularly spaced antenna elements. The direction of the beams can be steered by electrically controlling the phases of the radio frequency (RF) signals at active phase-shifting elements. However, the requirement of large-scale arrays and high transmission capacity results in the complexity of RF feed structures and a large number of phase-shifting elements. Latest developments in GaAs monolithic microwave integrated circuits (MMIC) technology have helped to reduce these engineering difficulties but still cannot fully satisfy the requirements for practical usage.

Phased array antennas using photonic radio frequency (RF) phase shifters hold great promise due to their many advantages such as simple implementation, optical distribution capability, low cost, low power consumption, small size, lightweight and immunity to electromagnetic interference [1]-[6]. Most importantly, in contrast to MMIC systems, the frequency bandwidth of these devices is very wide and effectively covers from DC to over 50 GHz. Also, it allows continuous beam forming without limitation on number of beam angles. Among the possible phase shifter architectures, the one described in [1] is the simplest and most flexible approach. In actual implementation, one can improve the performance with an advanced design and integrate multiple phase shifters in a single chip providing multiple independent phase outputs. In the following section, the detail engineering of these electrooptic polymer structures will be discussed.

## Operating Principle

Fig. 1 shows the advanced device architecture for the photonic RF phase shifter. It consists of a carrier-suppressed optical single-sideband (SSB) modulator embedded in one arm of a Mach-Zehnder (MZ) and an optical phase modulator on the other arm. When the SSB modulator unit is driven at quadrature as shown in Fig. 1, it typically generates a carrier at ? and a sideband at ? +? $_{RF}$ (point A). By inserting an additional balancing arm in the inner MZ, a carrier signal at ? from the SSB modulator can be suppressed (point B). The desired phase and magnitude of the optical signal in the balancing arm are established by the proper DC bias, $V_{Bal}$

and splitting ratio at the balancing arm, ?. On the other arm of the MZ, the control DC bias, $V_{Cont}$ is applied to the optical phase modulator to induce a phase shifted optical carrier at ?. Finally, the mixing of these signals in a photodiode gives rise to the RF signal at $?_{RF}$ with a variable phase controlled by $V_{Cont}$ (point C).

If the input optical signal with unit magnitude at a frequency of ? is $E_{in}(t) = e^{i?\,t}$, the expression for the output optical intensity at the modulation frequency $?_{RF}$ is given by,

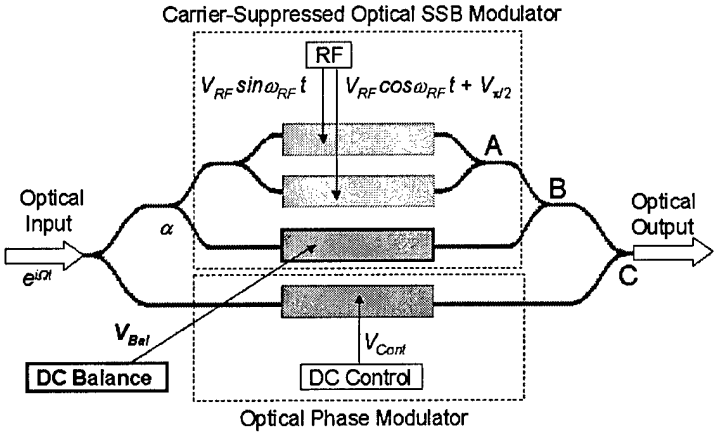


Fig. 1. The basic device architecture for the photonic RF phase shifter

$$I_{?_{RF}}(t) ? \frac{1}{4(1??)^2} A_{RF} J_1(?)\cos(?_{RF}t ?? ?_{RF}) \qquad (1)$$

where

$$?_{RF} ? \tan^{?1}\frac{?J_0(?)?2?\sin?_{Bal}?2(1??)\sin?_{Cont}?}{?J_0(?)?2?\cos?_{Bal}?2(1??)\cos?_{Cont}?} \qquad (2a)$$

$$A_{RF} ? \sqrt{?J_0(?)?2?\cos?_{Bal}?2(1??)\cos?_{Cont}?^2 ? ?J_0(?)?2?\sin?_{Bal}?2(1??)\sin?_{Cont}?^2} \qquad (2b)$$

Here $V_?$ is the half-wave voltage, ? = $??_{RF}/V_?$ is the modulation depth, $?_{Cont}$ = $??_{Cont}/V_?$ is the optical phase shift by the control DC bias, $?_{Bal}$ = $??_{Bal}/V_?$ is the optical phase shift by the balancing DC bias and ? is the optical power- splitting ratio at the balancing arm.

It can be seen from (2a) that the phase of the detected RF signal can be controlled by changes in control phase, $?_{Cont}$ (or control voltage, $V_{Cont}$). The balancing phase can be chosen to minimize the power fluctuation in (2b), which corresponds to 5?/4. This physically indicates that the balancing phase is set to be exactly opposite to the phase of the carrier signal from the SSB modulator unit. In addition, the RF power generated from the photodiode can be determined by (1) and turns out to be proportional to $A_{RF}^2$. The calculated RF phase and power characteristics are shown in Fig. 2 as a function of control voltage at a

modulation depth of 0.5. For the choice of ? ? $J_0(?)/\sqrt{2}$ with $?_{Bal}$ = 5?/4, the carrier signal from the SSB modulator is fully suppressed and the ideal characteristics for the RF phase and power can be obtained such that

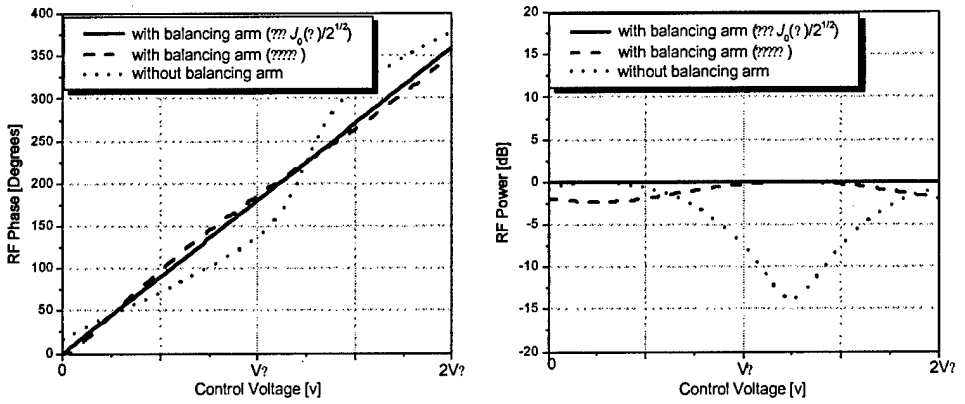


Fig. 2 The calculated RF phase and power characteristics as a function of control voltage at a modulation depth of 0.5

$$?_{RF} ? \tan^{?1}\frac{?2\sin?_{Cont}?}{?2\cos?_{Cont}?} ?? ?_{Cont}, \quad A_{RF}{}^2 ? const.$$

This indicates that the RF power does not vary at all and the RF phase shift is highly linear with respect to the control DC voltage, which makes these devices very suitable for optically controlled phase array antenna systems. Assuming a simple symmetric splitting at the balancing arm, i.e. ? = 1, with $?_{Bal}$ = 5?/4, this system shows a maximum phase deviation of less than 6? while maintaining the RF power fluctuation below 3 dB as the control voltage is tuned over $2V_?$. In this case, the carrier suppression in the SSB modulator is only partially accomplished since the balancing power is slightly unequal to the carrier signal from the SSB modulator unit. Nevertheless, this significant improvement of nearly one order of magnitude is capable of removing one of the major problems in using this type of phase shifter architecture. Note that for the case without the balancing arm (? = 0) it starts exhibiting a lack of linearity as the control voltage is tuned over $2V_?$. A maximum RF phase deviation of approximately 50? from the ideal linear characteristic is observed. In addition, the RF power exhibits fluctuation of approximately 15 dB as the control voltage is tuned over $2V_?$. Most of the detrimental effects are caused by the presence of the strong carrier signal that is not suppressed at all in the SSB modulator unit. This carrier signal is added to another phase shifted carrier signal at the same frequency ? and mixed with the sideband in the photodiode. The resulting RF signal reveals degradation of phase and power characteristics. For most

practical applications, a wide range of linear phase shifting is required and the RF power fluctuation is very undesirable.

## Multiple Output Photonic RF Phase Shifter in a Single Chip

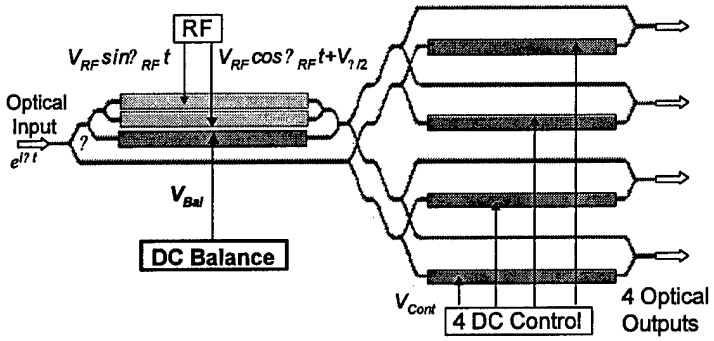


Fig. 3. The schematic diagram for the four-element RF phase shifter array in a single chip

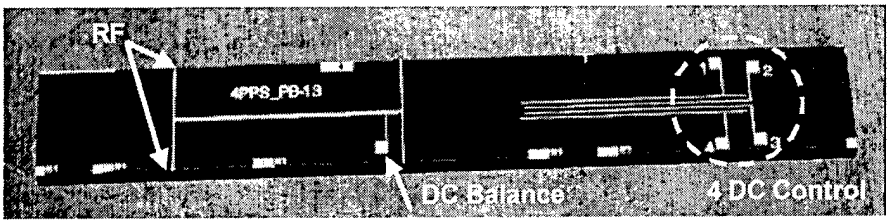


Fig. 4. The balanced multiple output photonic RF phase shifter fabricated in the APC-CPW polymer material

It is favorable to integrate multiple phase shifters in a single chip. This phase shifter array significantly reduces the complexity of RF feed structures and needs only a single RF and optical source. The four-element phase shifter array incorporating the balanced design is shown in Fig. 3. The modulated optical output from the balanced SSB modulator is split into four branches and combined with the four outputs from the optical phase shifters. This signal distribution in a planar chip can be achieved through the use of low crosstalk waveguide crossings. The performance of these devices could be severely impacted by that of the optical waveguide crossings and as such they need to be carefully implemented. Also, the additional propagation loss due to the array structure should be minimized. For this purpose, S-bend shape waveguides with very low bending losses can be implemented for all bending sections instead of regular corner-bend structure so that the device length can be minimized [7].

Fig. 4 shows the phase shifter array in a single chip fabricated using recently developed polymer materials and advanced polymer fabrication technologies as described before. The device size of the phase

shifter with four outputs was 3.8 cm ? 0.5 cm. For the simplicity of the design, the splitting ratio of the balancing arm, ?, was set to be 1.

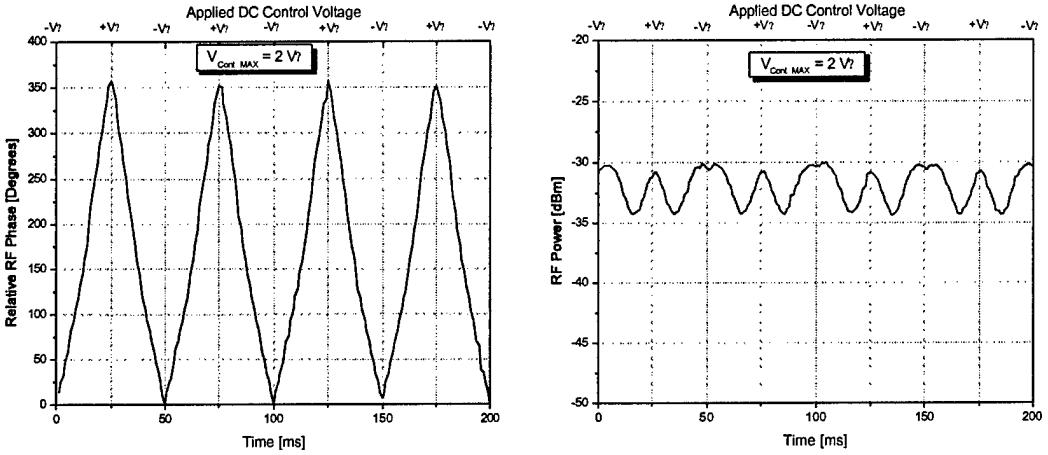


Fig. 5.The measured RF phase and power from a single output

The measured RF phase and power of a single element are shown in Fig. 5 at the modulation frequency of 20 GHz and the modulation depth of 0.58. Low frequency triangular waveforms of 50 Hz were used to drive the DC control arms instead of tuning the DC voltages manually. The linear relationship between voltage and time in the control triangular waveform enabled a one-to-one mapping between the measured RF phase (or power) and the control DC voltages. Therefore, the control voltage changes by amount of $2V_?$ for a period of 25 ms. For the control triangular waveforms of $2V_?$ (*?12V ~ +12V*), the RF phase was tuned by 360? with a high level of linearity and the RF power varied by less than 4 dB as expected from Fig. 2. Note that a single control of 360 ? of the RF phase shift corresponds to the half cycle of the voltage change in triangular waveforms in time domain (25 ms). Accordingly, Fig. 5 represent 8 times full operation within 200 ms. This performance can be even further improved by employing the design with the optional splitting ratio of the balancing arm as described before.

These RF phase shifters should contain the most important feature that the RF phases of an array element are independently controlled. In order to confirm this, four triangular waveforms of $2V_?$, set by the equal time delays, were applied to the four DC control arms. The measured RF phase characteristics are shown in Fig. 6. Almost identical

characteristics having the phase shift of 360? were observed for all output ports. It can be also seen from that, at a given time frame, this arrangement results in the same effect generated by four different voltages and consequently introduces the independent phase shifts at four output ports. In addition, the independent control of the RF phase was also demonstrated by applying the triangular waveforms having different peak-to-peak voltages to each control arm. The electrooptic polymer lends itself to these unique integrated systems since it can be easily processed and has extremely high nonlinearities.

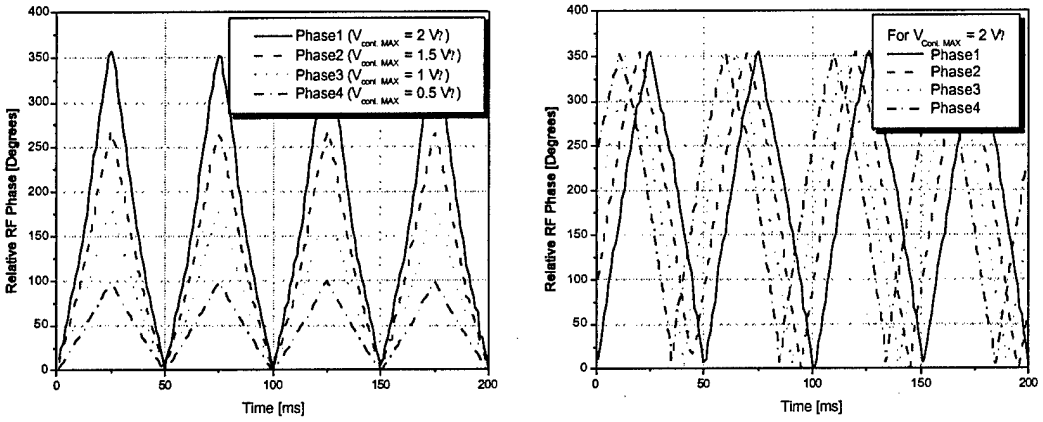


Fig. 6. The independently controlled four phase outputs

## REFERENCES


[1] D. K. Paul, "Optical beam-forming and steering for phased-array antenna", *Proc. IEEE Natural Telesys. Conf.* Jun 1993, p.7-12.

[2] Y. Kamiya, W. Chujo, K. Yasukawa, K. Matsumoto, M. Izutsu, and T. Sueta, "Fiber Optic Array Antenna Using Optical Waveguide Structure," *IEEE Int. Stymp. Dig., Antennas and Propagation*, vol. 2072, pp. 774-7, May 1990.

[3] J. F. Coward, T. K. Yee, C. H. Chalfant, and P. H. Chang, "A photonic integrated-optic RF phase shifter for phased array antenna beam-forming application", *Journal of Lightwave Technology*, vol. 11, no. 12, p. 2201-2205, Dec 1993.

[4] D. Jez, K. Cearns, and P. Jessop, "Optical Waveguide Components For Beam Forming in Phased-Array Antennas," *Microwave and Optical Technology Letters*, vol. 15, no. 1, 1997, pp. 46-49.

[5] J. M. Fuster, J. Marti, J. L. Corral, and P. Candelas, "Harmonic up/down-conversion through photonic RF phase shifters in phased-array antenna beam-forming applications", *Microwave and Optical Technology Letters*, vol.22, (no.4), Aug. 1999. p.247-9.

[6] S. R. Henion and P. A. Schulz, "Electrooptic phased array transmitter", IEEE Photonics Technology Letters, vol.10, March 1998. p.424-6.

[7] Jeehoon Han, B. Seo and H. Fetterman, "Integrated polymer photonic RF phase shifters for optically controlled beam forming systems", *Proceedings of IEEE MTT-S International Microwave Symposium (IMS2003)*, June 2003

## POLYMER MODULATOR PHASED ARRAY

**William H. Steier**
**University of Southern California**
**Los Angeles 90089-0483**

The USC effort include several experimental geometries which will greatly increase the capability of the next generation of devices. The use of coplanar guide structures have the potential of greatly increasing frequency response as well as lowing the $V_p$ of these polymer devices. New designs with integrated optical resonators open up the possibility of new configurations with DSP capability.

## A. New Electro-optic Polymers

During the past year we have received several new electro-optic polymers from the laboratories of Prof. Dalton and Prof. Jen at the University of Washington. One of the goals of this program is to bring these new materials into the device technology and demonstrate a low voltage high-speed polymer modulator. We have worked with LMAJ28/PQ-100 which is a basic dendritic structure chromophore in a polyquinoline host polymer. We have also received PSDA-AJL-4 polymer which is a reverse cross-link material. In this unusual material, the cross-linking opens at the poling temperature to allow easy alignment of the chromophores. The cross-linking then closes during the cooling cycle after the poling to provide high thermal stability.

In inserting a new core material into a working fabrication procedure, one often runs into technical problems. We have run up against several of these issues. Perhaps the most persistent has been the conductivity of these core materials at the poling temperature which has been higher than that of our typical cladding materials. In this case most of the applied poling voltage is across the higher resistance cladding and the poling efficiency is low. It has proven difficult to synthesize materials with a high EO coefficient and low optical loss and, in addition, low conductivity. To get around some of these problems we have initiated work on co-planar electrodes as described in Section C.

We have measured the optical loss at 1550 nm and 1310 nm for the EO polymers LMAJ28/PQ-100, PSDA-AJL-4, and PM-CF3-FTC3 (a side chain attached EO polymer) and found the loss to range from 1-3 dB/cm. This loss is low enough for device applications.

## B. Integrated Modulator/Antenna Element.

Work was started on the integration of a polymer modulator with a tapered slot antenna element. This is a joint project between USC and Photonics System Inc. This planar style antenna is designed to work from 8-12 GHz and will have a polymer Mach Zehnder modulator integrated into its base using hybrid integration. The goal of this first phase is to develop an interconnect technology between the antenna element and the modulator, to design a matching section between the transmission line on the modulator and the transmission line on the antenna element, and to measure the efficiency and frequency response of the integration. Based on these results, an integration approach to,

perhaps, fabricate the polymer modulator directly onto the antenna element will be considered.

In the first step in this program, USC supplied non-working modulator chips to Photonic Systems. These devices have the same electrode configuration and size as working modulators but were not poled. This allowed us to efficiently work out the interconnect technology without sacrificing working modulators. In this demonstration, microwave power was fed into one slot antenna, picked up by a second slot antenna that was connected to the electrodes of the modulator. The transmission from the input of the first antenna to the output of the modulator transmission line was measured. The results agreed with the theory and no unusual frequency response was measured over the operating range.

Working modulators have now been fabricated to integrate with the slot antenna elements. In this experiment, the received microwave power will be modulated onto the optical carrier and the complete antenna/modulator efficiency will be measured.

**C. Co-Planar Electrode Design**

Our standard traveling wave modulator is based on a micro-strip line design as shown in Figure 1.

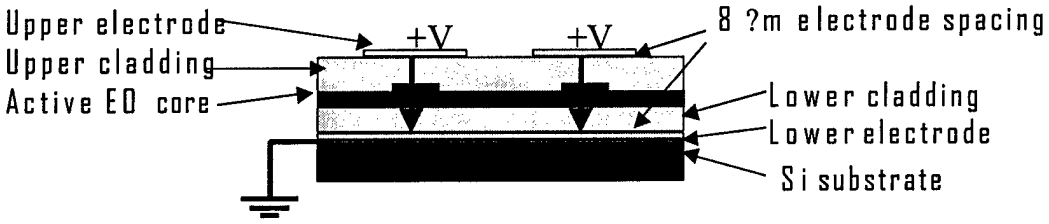


**Figure 1 Cross-section of the micro-strip line polymer modulator**

This design has the advantage that the spacing between the upper electrode and ground plane can be 8-9 ?m and this results in a low Vp. This spacing can be small because the optical beam in the triple stack(cladding/core/cladding) is elliptical in shape with a small vertical dimension. The beam is relatively tightly confined in the vertical direction by the index difference between the core and claddings and lightly confined in the horizontal direction by the ridge waveguide design. However this design has the disadvantage of requiring poling through the

triple stack which often results in poor poling efficiency as discussed in Section A. In addition, the microwave loss of the micro-strip line is typically 0.75dB/cm-$Hz^{1/2}$ and this is the limiting effect in the determining the 3 dBe bandwidth of the modulator.

Co-planar traveling transmission lines have traditionally been used in $LiNbO_3$ modulators because the lines must be fabricated on the surface of the $LiNbO_3$ crystal. We are now investigating the use of the co-planar lines in the polymer technology as shown in Figure 2.

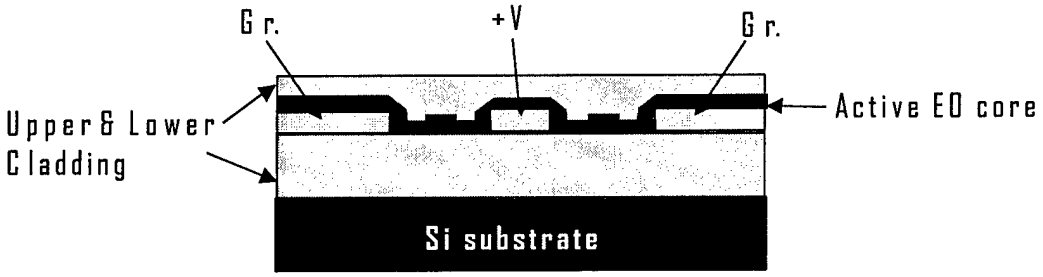


*Figure 2. Cross-section of the co-planar polymer modulator*

As seen in the Figure 2, there are no cladding materials between the EO polymer core and the electrodes in this design. We hope this will solve the poling efficiency problem discussed in Section A without requiring high resistivity EO polymers. In addition, co-planar transmission lines with losses as low as 0. 25dB/cm-$Hz^{1/2}$ have been reported in the literature. If we can reduce the loss by a factor of 2, the bandwidth for the same length device would increase by a factor of 4.

Often in the triple stack micro-strip line design we observe a bias instability. This instability results in a bias point that cannot be held stable and requires an increasing d-c bias voltage. To avoid this problem in the modulators supplied for the antenna integration we have used thermal biasing that has proved stable. Alternately we have bleached the modulators to the quadrature bias point. The voltage bias instability in the triple stack structure is believed to be due to the difference in the dc conductivity between the core and cladding polymers in much the same way the poling efficiency is limited. We therefore expect an addition advantage in the co-planar design of improved voltage bias stability. In our early results we have observed the improved stability.

We are now working out the fabrication approach for the co-planar design and working on understanding the issues involved in the in-plane poling. Our early results are promising but we have not built a working device. A new electrode mask set is now on order

**D. Controlled Bleaching of Mach Zehnder Modualtor to Set the Bias Point.**

We have demonstrated control of the bias point of the polymer Mach Zehnder modulators by controlled bleaching of one arm of the

interferometer. The bias point therefore does not require a bias voltage. Figure 3 shows the experimental set-up.

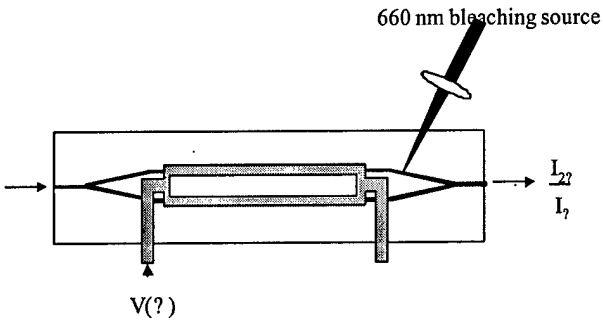


Figure 3. Bleaching to set the bias point in polymer modulator. The bias point is measured by observing the second harmonic of the low frequency modulation signal.

Figure 4 shows some typical results along with the bleaching power, beam size, and exposure time. The bias point can be set with an accuracy of a few degrees.

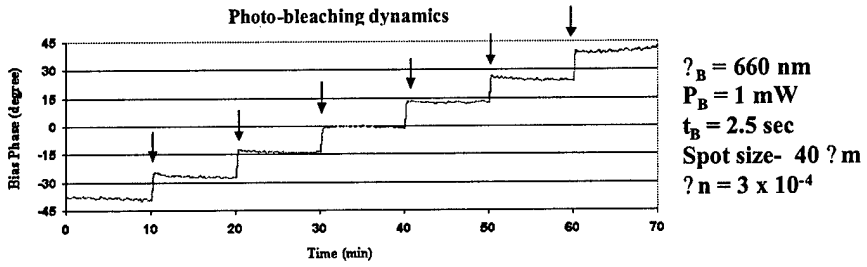


*Figure 4. The bleaching beam is turned on at the points indicated by the arrows for 2.5 sec. Exposure. There is some relaxation after the bleaching but a stable point is reached in ~ 1min.*

**E. Polymer Micro-Photonics**

We have extended our research into polymer micro-photonic components: a new class of devices with promising applications as modulators and wavelength filters for optically controlled radars. We have focused on waveguide ring resonators that consist of an optical waveguide formed into a ring integrated with input and output coupling waveguides. When the ring waveguide is made of low loss passive polymers, the device is a very high Q optical filter whose center wavelength can be temperature tuned or trimmed by photo-bleaching. When the ring waveguide is made of electro-optic polymers, the device is a compact, modest bandwidth modulator.

Figure 5 shows a ring resonator with the coupling waveguides. Using the notation shown in the figure and coupled mode theory one can derive the following results.

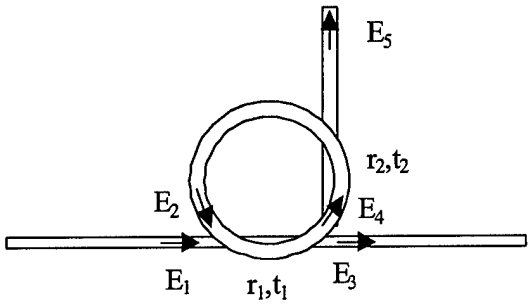


*Fig. 5 Model for the micro-resonator coupled to channel waveguides*

1. $$\begin{aligned} E_3 &? r_1 E_1 ? i t_1 E_2 \\ E_4 &? i t_1 E_1 ? r_1 E_2 \\ E_5 &? i t_2 E_4 \exp(i??_2) \end{aligned} \qquad (1)$$

where $|t_1^2|$ and $|t_2^2|$ are the amount of coupling. Also we can write:

2. $$\begin{aligned} E_2 &? r_2 \exp(???R)\exp(i??)E_4 ? r_2 a \exp(i2??)E_4 \\ a &? \exp(???R) \end{aligned} \qquad (2)$$

Where $?$ is the mode number, $R$ is the ring radius and $?$ is the total loss in the ring given by:

$? ??_m??_b??_w$

$?_m$= material loss coefficient

$?_b$= radiation loss coefficient due to bending

$?_w$= radiation loss coefficient due to wall roughness

By solving (1) and (2) we obtain:

3. $$\frac{I_5}{I_1} ? \frac{|t_1|^2 |t_2|^2}{1 ? 2r_1 r_2 a \cos(2??) ? r_1^2 r_2^2 a^2} \qquad (3)$$

Next let's define and calculate some parameters, which are important for micro-resonators. The first parameter is the Q of the micro-resonator, which is defined by:

4. $$Q ? \frac{?_0}{??_{1/2}} ? \frac{\nu_0}{?\nu_{1/2}} \qquad (4)$$

where $??_{1/2}$ is the full bandwidth at half maximum of the dropped power or transmitted power. To calculate $?\nu_{1/2}$ using similar approach for Fabry-Perot resonators [11] we can obtain:

$$Q ? \frac{\sqrt{r_1 r_2 a} L ? n_g}{(1 ? r_1 r_2 a) ?_0} \qquad (5)$$

where $n_g$ is the group index given by:

$$n_g(?) ? n_e(?) ? ? \frac{dn_e(?)}{d?} \qquad (6)$$

Equation 5 specifies the loaded Q of the resonator. If we are considering the unloaded Q we can replace $r_1$ and $r_2$ by 1. Also since we have:

$$1 ? a ? 1 ? \exp(?? L/2) ? ? L/2 \qquad (7)$$

We can obtain this equation for unloaded Q:

$$Q ? \frac{2? n_g}{?? _0} \qquad (8)$$

It is important to note that the Q is not a function of the length of the device. Also it is interesting to know that with 1dB/cm loss a Q of more than $10^5$ is possible.

Next we consider free spectral range (FSR), which is basically the distance between the peaks in the resonator. To calculate the FSR we consider that the resonance frequency of the mode number $?$ can be specified by:

$$?? \frac{n_{eff}(?_m) L}{?_m}, ?? 1 ? \frac{n_{eff}(?_{m?1}) L}{?_{m?1}} \qquad (9)$$

So the free spectral range is simply:

$$FSR ? ?_{m?1} ? ?_m ? \frac{?^2}{n_g(?) L} \qquad (10)$$

Finally another important parameter for the micro-resonator is the finesse. The finesse is defined and calculated (approximately) for unloaded case as:

$$f ? \frac{FSR}{?? _{1/2}} ? \frac{2?}{?L} ? \frac{1}{?R} \qquad (11)$$

Passive micro-resonators

The minimum size of the ring resonator is determined by the index difference between the core and the cladding to keep the radiation leakage from the ring waveguide small. Table 1 shows the properties of the polymer materials we have available.

Table 1: The refractive index and the loss of the polymers used.

| Material | Index 1300nm | Loss (dB/cm) 1300nm | Index 1550 nm | Loss (dB/cm) 1550nm |
|---|---|---|---|---|
| SU-8 | 1.567 | 0.53 | 1.565 | 4 |
| NOA 61 | 1.545 | 0.33 | 1.541 | 1.1 |
| UFC170 | 1.490 | 0.53 | 1.488 | 3 |
| UV15 | 1.510 | 0.89 | 1.504 | 4.2 |
| Teflon AF 1601 | 1.300 | - | 1.297 | - |
| CLD1 | 1.614 (TE) | 0.95 | 1.612 (TE) | 1.69 |

We have fabricated two different sets of ring resonators. In one set we have used an index difference between the waveguuide core and the claddings of 0.1. To keep the radiation leakage from the ring waveguide small, the devices are relatively large (550?m in diameter). For smaller diameter rings (50?m in diameter), we have fabricated devices with an index contrast of 0.3. The coupling into and out of the rings is to wavguides fabricated above the rings. Since the polymer technology is a spin technology, it is reasonably easy to fabricate 3D structures[2]. The fabrication of the resonator is very similar to our standard polymer device fabrication and Fig. 2 shows the fabrication procedure.

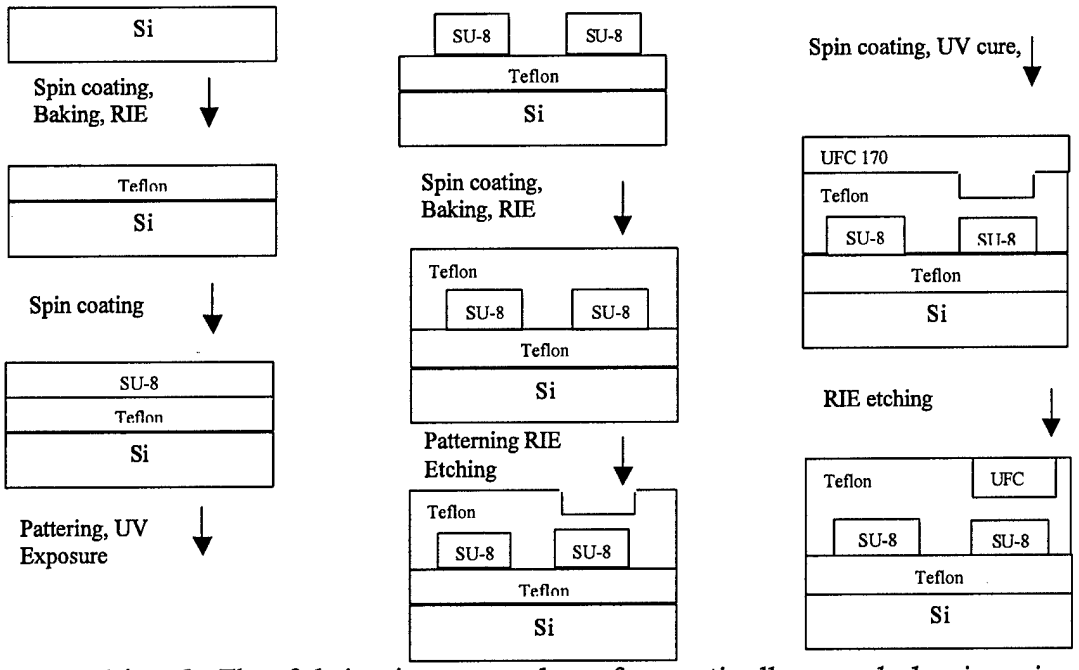


*Fig. 6. The fabrication procedure for vertically coupled micro-ring resonators.*

The fabrication of the device starts with spin coating Teflon on silicon substrate. Using 11% solution of Teflon AF 1600 in 3M FC-40 solvent [3] we spin coat 2.8 ?m Teflon. Next we etch this layer using RIE for 2 minutes in oxygen. This etching is required to change the surface properties of Teflon since the adhesion to Teflon is very poor. In the next step a 1.5 ?m SU-8 [3] layer is spin coated on the substrate. SU-8 is a photo-resist which is patterned using the photo-lithography to form the micro-ring. In the next step a 4.5 ?m Teflon layer is spin coated on the device. This process also planarizes the sample. The Teflon layer is etched for 2 minutes to improve the adhesion for the following step of the process. The Teflon layer is patterned using photo-resist and etched to form trenches for the channel waveguide. Next a UFC 170 A [3] layer is spin coated on the device and cured using UV exposure and baking to fill out the trenches formed in the previous step. In the next step the slab part of UFC 170 layer is removed using RIE etching. Finally the device is cut using dicing saw. Fig. 7 shows the device cross-section and the top picture of the fabricated device.

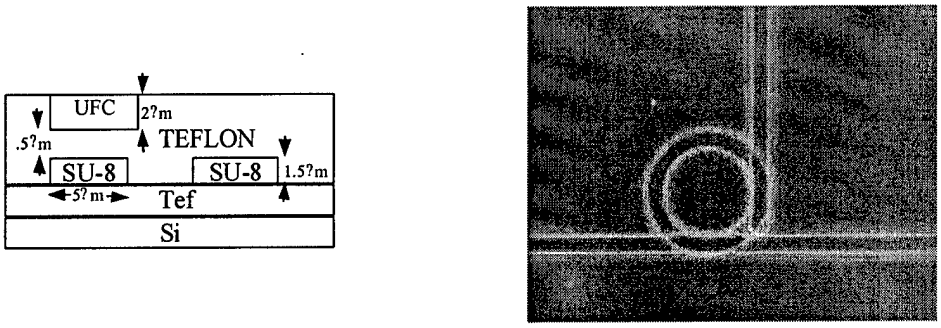


*Fig. 7. The cross section schematic and the fabricated device picture*

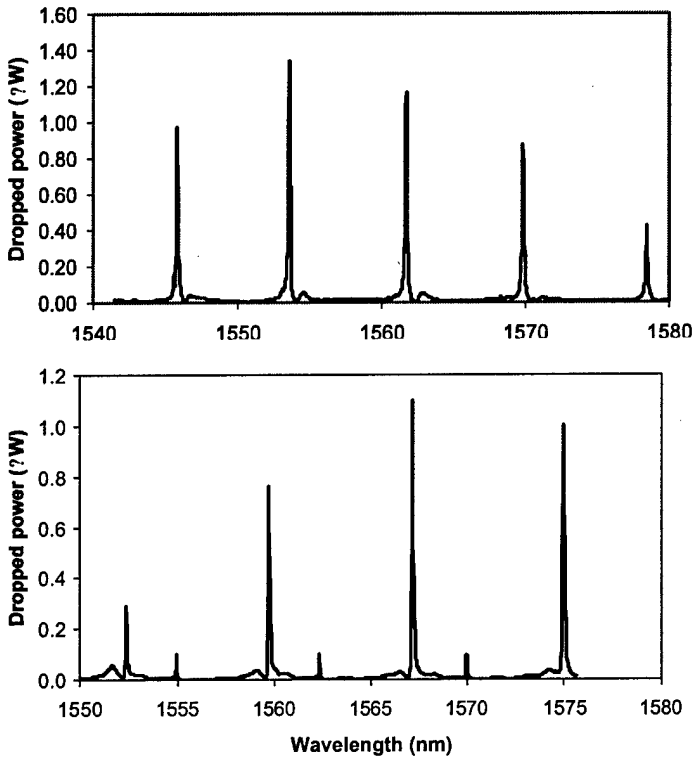


*Fig. 8. Drop port response as a function of wavelength (a) 55?m diameter (b) 64 ?m diameter*

* Excluding material loss

| Index difference | Device Diameter | FSR (nm) 1300nm | Finesse 1300nm | Loss* (dB/cm) | FSR 1550nm | Finesse 1550nm | Loss* (dB/cm) |
|---|---|---|---|---|---|---|---|
| 0.3 | 64?m | 5 | 141 | 9.03 | 7.5 | 117 | 7.5 |
| 0.3 | 55?m | 5.4 | 92 | 16.58 | 8.1 | 84 | 14.7 |
| 0.1 | 440?m | 0.8 | 80 | 1.93 | | | |
| 0.1 | 660?m | | | | 0.8 | 20 | 2.56 |

Table 2: The measured FSR and finesse for different devices

Fig. 8 shows the measured power in the drop port for different size devices. Table 2 summarizes the measured device performance for different size devices. As shown, the smaller devices have lower Q's but higher finesse. A finesse as high as 140 for 1300nm and 120 for 1550 is obtained. Since these devices are all under coupled, the Q is largely determined by the waveguide loss and this can be calculated. As it is seen from the table with a fixed index contrast the smaller devices exhibit larger loss. This is probably due to the larger value of the electro-magnetic field at the boundary between the core to cladding which results in larger scattering loss.

Refractive indexes of polymers have a large thermal dependence. Hence one can use this to tune the resonant wavelength of micro-resonators made out of polymers. Fig. 9 shows the thermal tuning of the micro-resonators we have fabricated. As it is seen from the figure the resonance wavelength can be tuned 5nm by 40?C. It is easily possible with a larger temperature range to achieve 10 nm tuning

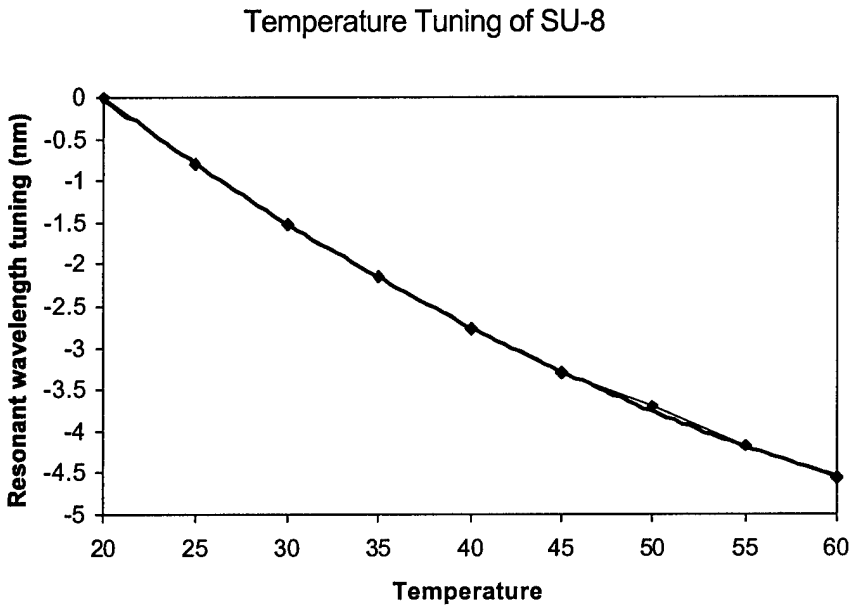


*Fig .9 Temperature tuning of the micro-resonator filter.*

Active micro-ring devices

A very small change in the refractive index of the high Q micro-ring can cause a large change in the output of the device as shown in Fig 10.

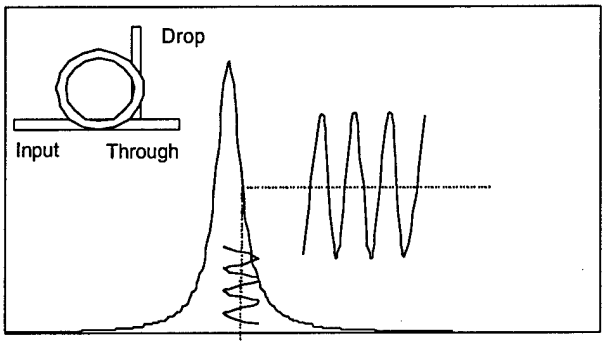


*Fig. 10. The modulation concept based on the resonator.*

Hence we can use the small change in refractive index caused by electro-optic effect to modulate the light in the micro-resonator. The schematic of a fabricated device is shown in Fig. 11 and is similar to the passive devices except for the electro-optic material in the core and the gold electrodes.

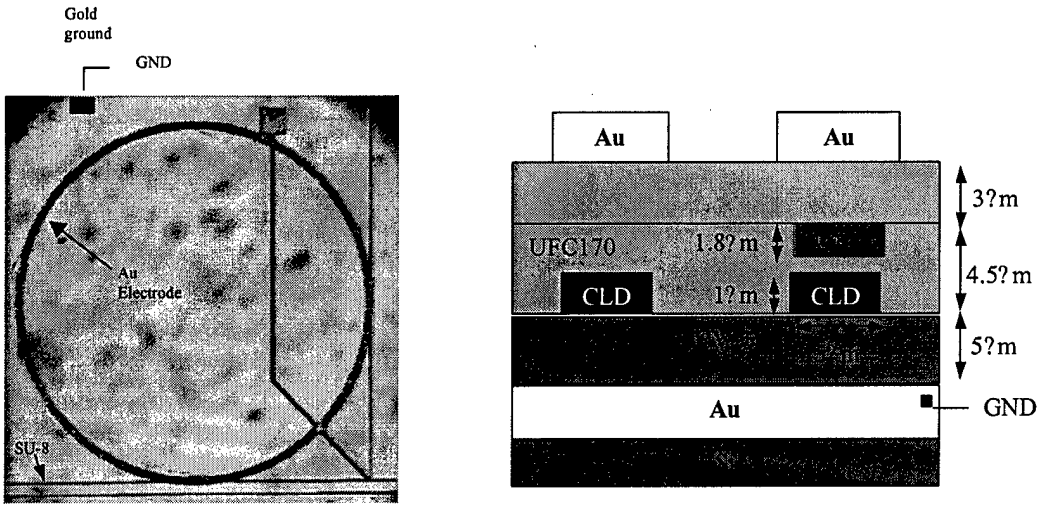


*Fig.11. The cross section schematic and the fabricated modulator device picture. (The background is the bottom gold electrode)*

The refractive indexes of the materials used in the device are summarized in Table 1. CLD1/APC [4][5] is used as the material for the micro-ring. The device fabrication is similar to passive structures except for the electrodes and the polling required in this case. The fabrication starts with Au coated Si substrate. A 5?m UV-curable epoxy UV15 (from master bond Co.) is used as the lower cladding. The 5.0?m thickness is required to ensure negligible plasmon loss due to the bottom Au electrode. A 1?m CLD1/APC layer is coated and etched using RIE in oxygen to form a channel waveguide in the form of a micro-ring. The width of the ring waveguide is 5?m. Different radius rings are fabricated on the same substrate. Based on the calculation and measurement, the radiation loss is negligible for devices larger than 300?m in radius for 1.55?m and 200?m for 1.3?m assuming a CLD1 core and UFC170 cladding. Next a middle cladding of UFC-170 is spin coated on the device. The thickness of this layer, which determines the distance between the ring and channel waveguides is 4.5 ?m. This also planarized the device. Two channel waveguides are made on top of the micro-ring as the input and output channel waveguides. To do this, the UFC-170 layer is first patterned in the form of a waveguide. Next the required depth is etched into the UFC-170. On the next step SU-8 is used as the material for the channel waveguide. The effective refractive index of SU-8 waveguide matches the effective refractive index of the whispering gallery mode of the CLD1/APC micro-ring and efficient coupling is therefore achieved. By spin coating SU-8 an inverted ridge waveguide is formed. The slab region of the ridge waveguide is removed by RIE etching. Next a 3?m upper cladding is spin coated on the device and the device is polled using corona polling. The polling temperature was 145 ?C and the

applied voltage was 10kV. The sample was polled for 30 minutes. An upper gold cladding is deposited and patterned on the device to cover the micro-ring. The device is cut using dicing saw. Fig.7 shows the fabricated device picture. The top and bottom gold layer in addition to the waveguides can be seen from this picture.

The device was tested using lensed fiber as the input and output waveguide. A tunable New Focus laser at 1.3?m and 1.55 ?m was used as the source. Fig. 12 shows the drop port power as a function of change of the input laser frequency for a 1500?m diameter device at zero bias.

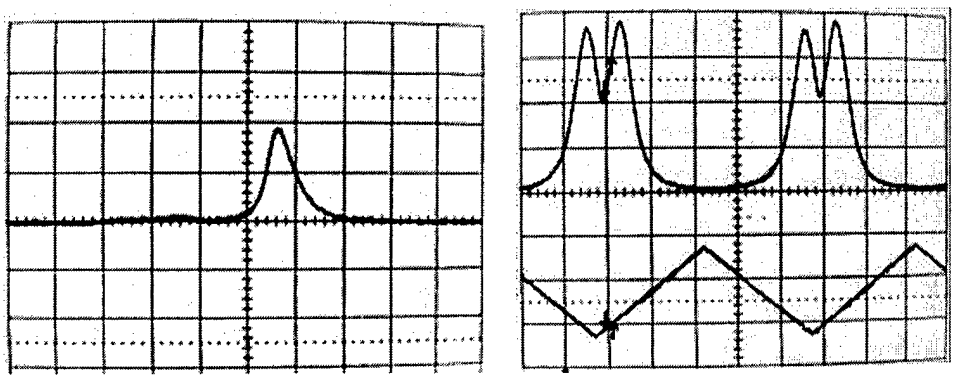

(a) (b)

*Fig. 12 (a) The optical frequency response of the fabricated modulator device at zero bias. (b) The applied voltage to the electrodes of the device and the modulated output intensity at 1300nm for a 1500?m diameter device at a fixed wavelength.*

As can be seen from this figure for 1300nm the FWHM bandwidth of the device is approximately 4GHz for TM. (TM is defined as the electric field perpendicular to the device surface). Hence the Q of the device is $6.2 \times 10^4$. The calculated loss based on the measured Q for this device is 5.2 dB/cm. The Q of the device for 1.55?m is almost half the values at 1.3?m. Next the laser wavelength is fixed and a low frequency saw-tooth voltage is applied to the electrodes of the device. Fig 78(b) shows the modulated signal at the drop port of the device. Since $V_{??}$ cannot be defined for this device we can define a voltage that shifts the resonance by the FWHM. This is measured to be 4.86 volt for 1300nm and corresponds to an $r_{33}$ of 33pm/V. This is lower than the $r_{33}$ (50pm/V at 1300nm) for same material achieved in conventional Mach-Zehnder devices. This is probably due to reduced poling efficiency. The FWHM voltage for 1.55?m for this device is 16V. Similar results for smaller devices are obtained. For a 300?m radius device the FWHM voltage is measured to be 9 V at 1300nm. This voltage is higher partly because the device Q is slightly lower ($4.7 \times 10^4$ and $5.8 \times 10^4$ for TM and TE respectively) and also because the confinement of the mode is smaller in

the micro-ring due to larger curvature. The FSR for this device is 0.9nm.

The frequency response of traveling wave Mach Zehnder polymer electro-optic modulators are limited by the RF loss of the micro-strip line. Since the micro-ring devices are much smaller than the microwave wavelength (even up to 100GHz) the device high-speed behavior is limited by the capacitance of the electrode. For devices smaller than 500?m in diameter, the electrode capacitance does not limit the frequency response. However there is an optical limit for high-speed modulation. This limit comes from the fact that there is a finite life-time for the photons in the resonator. If the modulation bandwidth of the device is defined as one half of the optical FWHM bandwidth(as typically done in resonant devices):

BW=?? ???? ????

The required voltage to change the output from the maximum to half maximum can define the sensitivity of the device. The index change required to achieve half maximum is:

12. $$\frac{?n_e}{n_e} ? \frac{??_{1/2}}{?} \quad (13)$$

Where $n_e$ is the effective index of the micro-ring and $?$ is the optical frequency. Finally using the index change relation for electro-optic material given by:

13. $$?n_e ? \frac{1}{2} k n^3 r_{33} \frac{V}{d} \quad (14)$$

Where $k$ is the confinement factor, $V$ is the applied voltage, $n$ is the refractive index of the electro-optic material and $d$ is the distance between the electrodes. One can obtain the ratio of the bandwidth to the switching voltage as:

14. $$\frac{BW}{V} = \frac{k u n^3 r_{33}}{2 n_e d} \quad (15)$$

This is a reasonable quantity to define the properties of the modulator. For the electro-optic polymers we have used (CLD1) and assuming a confinement factor of 90% and a distance of 3?m between electrodes (index contrast of 0.3 between the core and cladding required) the ratio of 4 GHz/V for 1300nm is achievable. For 1550nm the ratio is 2.5 GHz/V.

For our device since the FWHM optical bandwidth is 4GHz the maximum modulation bandwidth is 2GHz. The high-speed measurements confirm this. Higher bandwidth devices can be fabricated but they would require higher driving voltage to achieve the same

modulation depth. Only by using materials with higher $r_{33}$ it is possible to achieve higher bandwidth and maintain the same voltage.

A relatively clear eye diagram up to 1GB/sec is obtained for this device as shown in the Fig. 13 by applying 1V data stream. The extra noise is due to instability since the device is not packaged. The bandwidth of the device is measured to be 2GHz, which is consistent

with our prediction.

*Fig. 13. The eye diagram of data transmission using the fabricated modulator at 1GB/sec at 1300nm for a 1500?m diameter device*

**Publications During Period**

Book Chapters

1. " Polymer Microring Resonators", with P. Rabiei, *Optical Microcavities*, K. Vahala editor, World Scientific Co., 2004
2. "Polymers in Photonic Devices", with H. R. Fetterman, Alex Jen editor, Wiley and Sons,2004

Journal articles

1. H-C Song, M-C Oh, S-W Ahn, W. H. Steier, H. R. Fetterman, C. Zhang, "Flexible Low Voltage Electro-optic Polymer Modulators", Appl. Phys. Lett. **82**, 4432-4, June 23, 2003
3. P. Rabiei, W. H. Steier, "Tunable Polymer Double Micro-ring (DMR) Filters", IEEE Phot. Tech. Lett., **15**, pp 1255-7, (2003)
4. D. H. Chang, T. Azfar, S-K Kim, H. R. Fetterman, C. Zhang, W. H. Steier, "Vertical adiabatic transition between silica planar waveguide and electro-optic polymer fabricated using grayscale lithography" Optics Lett., **28**, pp. 869-871 (2003)

5. S. Kim, K. Geary, D. Chang, H. Zhang, C. Wang, W. Steier and H. Fetterman "TM-pass Polymer Modulators with Poling-induced Waveguides and Self -Aligned Electrodes" Accepted for publication in IEEE Phot. Tech. Lett.
6. S-K Kim, H. Zhang, D, H. Chang, C, Zhang, C. Wang, W. H. Steier, H. R. Fetterman, "Electrooptic Polymer Modulators With an Inverted-Rib Waveguide Structure", IEEE Phot. Tech. Lett., 15, p 218-220, (2003)
7. S-K Kim, K. Geary, H. R. Fetterman, C. Zhang, C. Wang, W. H. Steier, "Photo-Bleaching Induced Electro-optic Polymer Modulators with Dual Driving Electrodes Operating at 1.55 ?m Wavelength", Electr. Lett., 39, 1321-3, (2003)
8. "Low Loss Interconnection between Electro-optic and Passive Polymer Waveguides with a Vertical Taper", M-C Oh, C. Zheng, H-J Lee, W. H. Steier, H. R. Fetterman, IEEE Phot. Tech. Letters, **14**, 1121 (2002)
9. C. Zhang, C. Wang, J. Yang, L. R. Dalton, G. Sun, H. Zhang, and W. H. Steier, "Electric-Poling and Relaxation of Thermoset Polyurethane Second-Order Nonlinear Optical Materials: The Role of Cross-Linking and Monomer Rigidity," Macromolecules, 34, 235-43 (2001).
10. C. Wang, C. Zhang, C. Zhou, M. Chen, L. R. Dalton, H. Zhang, W. H. Steier, "Urethane-Urea Copolymers Containing Siloxane Linkages: Enhanced Temporal Stability and Low Optical Loss for Second-Order Nonlinear Optical Applications," Macromolecules, 34, 2359-63 (2001)
11. C. Zhang, L. R. Dalton, M.-C. Oh, H. Zhang, and W. H. Steier, "Low $V_?$ Electrooptic Modulators from CLD-1: Chromophore Design and Synthesis, Materials Processing, and Characterization," Chem. Mater., 13, 3043-50 (2001).
12. J. H. Kim, L. Sun, C.-H. Jang, D. An, J. M. Taboada, Q. Zhou, X. Lu, R. T. Chen, X. Han, S. Tang, H. Zhang, W. H. Steier, A. Ren, and L. R. Dalton, "Polymeric Waveguide Beam Deflector for Electro-Optic Switching," Proc SPIE, 4279, 37-44 (2001).
13. D. H. Chang, H. R. Fetterman, H. Erlig, H. Zhang, M-C Oh, C. Zhang, W. H. Steier, "39 GHz optoelectronic oscillator using broad-band polymer electro-optic modulator", IEEE Phot. Tech. Lett. **14**, pp191-3(2002)
14. J. Han, H. Erlig, D. Chang, M-C Oh, H. Zhang, C. Zhang, W. H. Steier, H. Fetterman, "Multiple Output Photonic RF Phase Shifter Using a Novel Polymer System", IEEE Phot. Tech. Lett. V. **14**, p531-3 (2002)
15. P. Rabiei, W. H. Steier, C. Zhang, L. R. Dalton, "Polymer Micro-ring Filters and Modulators" IEEE J. Lightwave Technology, **20**, 1968-75 (2002)

16. P. Rabiei, W. H. Steier, C. Zhang, L. R. Dalton "Micro-photonic Polymer Devices (Invited), International Optical Communication, Aug. (2002)
17. S-W Ahn, W. H. Steier, Y-H Kuo, M-C Oh, H-J Lee, C. Zhang, H. R. Fetterman, "Integration of electro-optic polymer modulators with low-loss fluorinated polymer waveguides" Optics Letters, **27**, 2109 December (2002)
18. Hua Zhang, M-C Oh, A. Szep W. H. Steier, C. Zhang, L. R. Dalton, H. Erlig, Y. Chang, D. H. Chang, H. R. Fetterman, "Push Pull Electro-optic Polymer Modulators with Low Half-Wave Voltage and Low Loss at both 1310 nm and 1550 nm" Appl. Phys. Lett. **78**, p3116 –8 (2001)
19. M-C. Oh, H. Zhang, A. Szep , W. H. Steier, C. Zhang, L. R. Dalton, H. Erlig, Y. Chang. Boris Szep, H. R. Fetterman, "Recent advances in electro-optic polymer modulators incorporating phenyltetraene bridged chromophore " (Invited) J. Quant Electr. Sel. Topics on Organics for Photonics, **7**, pp826-35,(2001)

Presentations

1. "Electro-Optic and Passive Polymer Micro-Resonators" (Invited), William H. Steier, P. Rabiei, H-C. Song, B. Bhola, H. Tazawa, Y-K Kuo, IEEE/LEOS Summer Topical Meeting, San Diego, CA, June, 2004.
2. "Polymer Waveguide Devices"(Invited) W. H. Steier, H. C. Song, Y.H. Kuo, P. Rabiei, S_W Ahn, M-C Oh, H. R. Fetterman, C. Zhang, L. R. Dalton, A. K. Jen. SPIE, San Jose, CA, Jan. 2004.
3. "Polymer Electro-optic Devices and Systems" (Invited), William H. Steier, American Association for the Advancement of Science Annual Meeting, Feb. 15, 2004, Seattle, WA.
4. "Advances in Polymer Waveguide Devices"(Invited) W. H. Steier, H. C. Song, Y.H. Kuo, P. Rabiei, S_W Ahn, M-C Oh, H. R. Fetterman, C. Zhang, L. R. Dalton, A. K. Jen. LEOS 2003, Tucson Az.
5. "Polymer micro-ring modulator with 1 THz FSR", P. Rabiei, W. H. Steier, C-K Wang. Post deadline paper, CLEO, Long Beach, CA, May 23, 2002
6. "Micro-ring resonators using polymer materials", P. Rabiei, W. H. Steier, Paper WO5, LEOS, San Diego, Nov. 2001.
7. "Integrated WDM polymer modulator", P. Rabiei, W. H. Steier, C. Zhang, L. R. Dalton, Paper TuF6, Optical Fiber Conf. Anaheim, CA, March 2002.
8. " Polymeric optical waveguide modulators and their applications" (Invited) W. H. Steier, M-C. Oh, H. Zhang, A. Szep, Y. H. Kuo, P. Rabiei, S. W. Ahn, L. R. Dalton, C. Zhang, H. R. Fetterman, D. H. Chang, H. Erlig, B. Tsap, Paper CMI3, CLEO/QELS, Long Beach. CA, May, 2002

## L. Dalton
## USC and University of Washington

This portion of the research was to develop new materials that would support the phased array program. An effort was made to develop polymers with higher electrooptic coefficient and high temperature operation for military applications.

The Funding in this portion of the effort was used to support postdoctoral researcher Dr. Cheng Zhang, who has systematically explored the modification of the chromophore CLD. Many structural variants of CLD have been prepared and sufficient quantities were prepared to permit fabrication and evaluation of a number of prototype devices. Most research has focused on the exploration of CLD type chromophores into the commercially available (Aldrich); however, researchers at the University of Washington provided Dr. Zhang information that permitted Dr. Zhang to explore the use of new crosslinking reaction chemistry described in the accompanying figure.

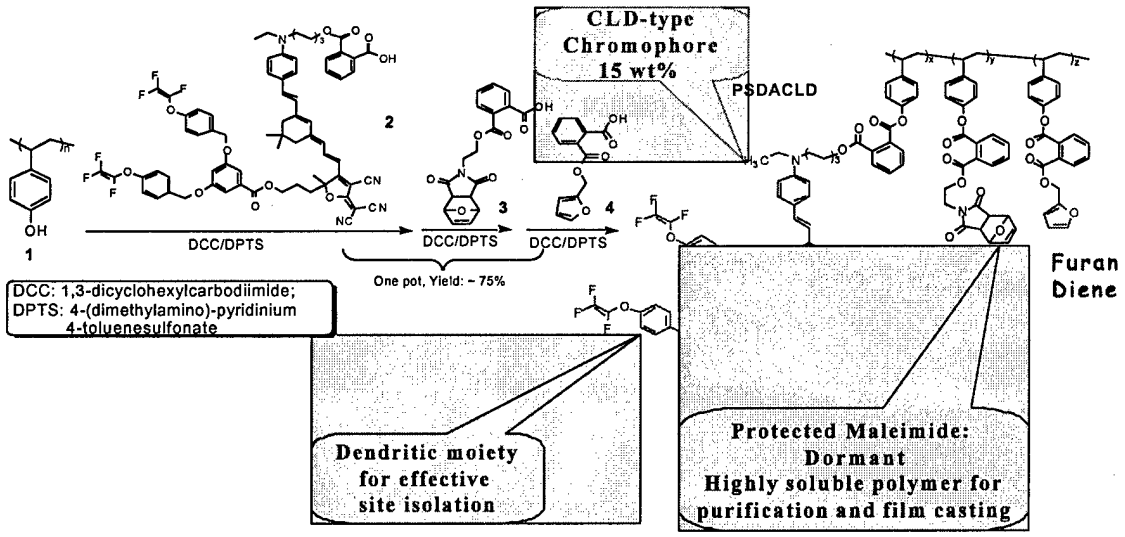


These crosslinking reactions based on reaction of the trifluorovinylether moiety to form cyclobutyl crosslinks and upon Retro Diels Alder chemistry permit improved thermal and photochemical stability to be realized.

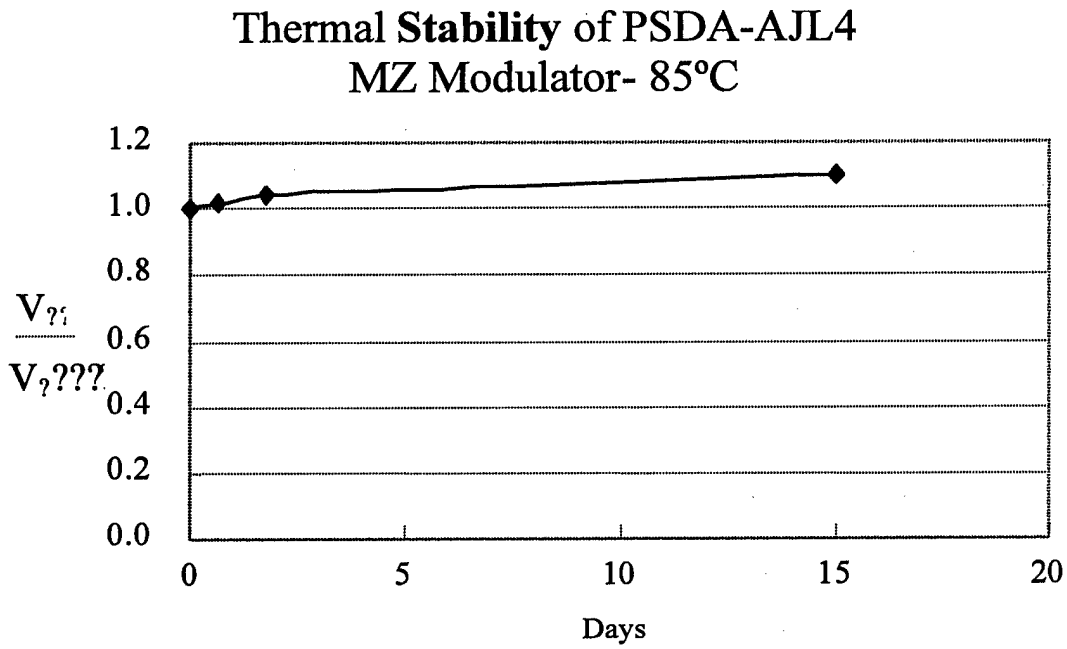


The above data was obtained by Prof. William Steier on samples provided by Professor Alex Jen. With support from an AFOSR single investigator grant, Professor Dalton and students at the University of Washington have developed new chromophores that exhibit substantially improved second order optical nonlinearity relative to CLD. As shown in the accompanying table, the experimentally observed trend is consistent with predictions of DFT calculations.

| Designation/ HOMO-LUMO Gap | Structure | ?/D | $?_{HRS}$ /$10^{30}$esu | $?_{zzz}$ /$10^{30}$esu |
|---|---|---|---|---|
| CLD 1.119 eV | 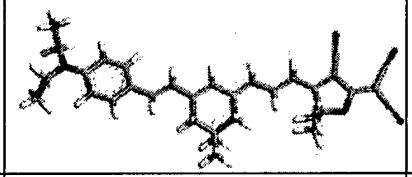 | 29.1 | 146 | 293 |
| D1B2A3 0.923 eV | 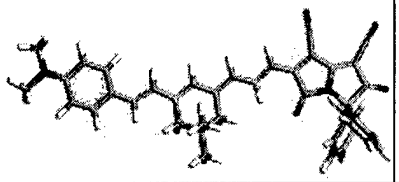 | 26.8 | 211 | 402 |
| D1B2A4 0.845 eV | 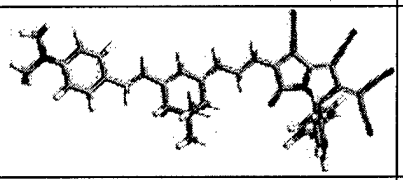 | 32.3 | 223 | 454 |
| D1B9A3 0.815 eV | 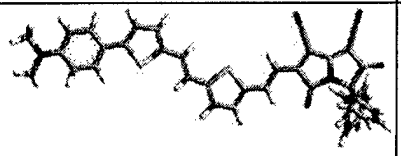 | 25.3 | 500 | 990 |
| D1B9A4 0.736 eV | 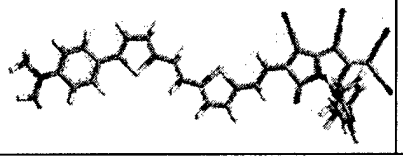 | 31.1 | 585 | 1214 |

**New chromophores should permit electro-optic coefficients of 300 pm/V to be achieved at telecommunication wavelengths.**

Photonic Systems :

**Integration of Wideband Printed Antennas and Polymer Modulators**

R. Waterhouse[1], H. Roussell[1], R. Nelson[1], C. Cox[1] and W. Steier[2]

[1]Photonic Systems Inc.
Massachusetts, USA

[2]University of Southern California
California, USA

## I Introduction

Efficient integration of antennas with photonic and microwave modules has long been sort after as this art can be considered as the enabling technology that would finally allow all the advantages of photonic/fiber optic systems to be utilized in radar applications. Research to date on this endeavor has been somewhat sporadic due to the complexity of the problem and the multidisciplinary skills required to resolve all the potential issues related to efficient antenna/microwave/photonic integration.

Of all the forms of radiating elements, printed antennas are the most compliant with the requirements for efficient integration with microwave and photonic devices. These antennas have compatible structural properties with transmission line technologies used to realize microwave and photonic circuits. Printed antennas can even allow for direct integration; namely, they can be implemented on the same material used to fabricate the microwave and photonic devices. However in their conventional form, printed antennas fabricated on typical high permittivity OEIC (Optoelectronic Integrated Circuits)/MMIC (Microwave Monolithic Integrated Circuits) materials can suffer from a very narrow impedance bandwidth thereby countering one of the advantages of using an optical fiber distribution scheme. Also, surface wave effects can severely degrade the efficiency of the printed antenna, diminishing the performance of the overall microwave/photonic link. The excitation of surface waves not only reduces the efficiency of the radiator, but can also cause unwanted coupling between the devices within the module [1].

We have previously investigated several techniques to integrate antennas with photonic devices. These methods were based on hybrid integration and direct integration and photographs of the integrated modules are shown in Figures 1a and 1b, respectively [2, 3]. For hybrid integration, each photonic/RF/antenna function is designed and developed preferably using planar technology on an optimized combination of materials. These 'islands' of optimized functions are then interconnected via small sections 50 ? transmission lines and a series of bond wires. Some of the advantages of the indirect integration technique are obvious but it is worth spelling them out. Importantly, this form of indirect integration allows for each functional block of the module to be developed relatively independently of the other components. For example, the photodiode can be developed on material with a high optical/electrical coefficient independently of the antenna as long as each component has input (and/or output) ports matched to a specified impedance, typically 50 ?. Such a procedure allows for well-established practices to be undertaken for the design and development of the individual

components. There are however some drawbacks of this technique including the larger size of the terminal (compared to direct integration), the labor-intensiveness of the integration process and the loss associated with the interconnections, namely the bond-wires and the small sections of transmission lines. This loss is not trivial and can cause degradation in the system performance.

Direct integration is where all the functions utilize a common material and so the issues associated with the development of small, independent transmission line sections discussed earlier are avoided. However, this is not a trivial task, for example, consider an integrated antenna-photonic module incorporating Lithium Niobate ($LiNbO_3$) as the material for the E/O converter. To use this material in an OEIC approach can yield a very inefficient antenna, simply because of the high dielectric constant of $LiNbO_3$. However, by using a two element radiating structure, where one radiator resides on the high dielectric constant material and the other on a low dielectric constant laminate, highly efficient and broadband antennas can be formed. Although direct integration overcomes some of the issues associated with indirect integration there are still some problems with this technology. Firstly, typically large wafers are required to accommodate for the foot-print of the entire module. Secondly, the design procedures for each sub-component now become difficult as the designer has lost one of their degrees of freedom, namely the choice of material (dielectric constant and thickness).

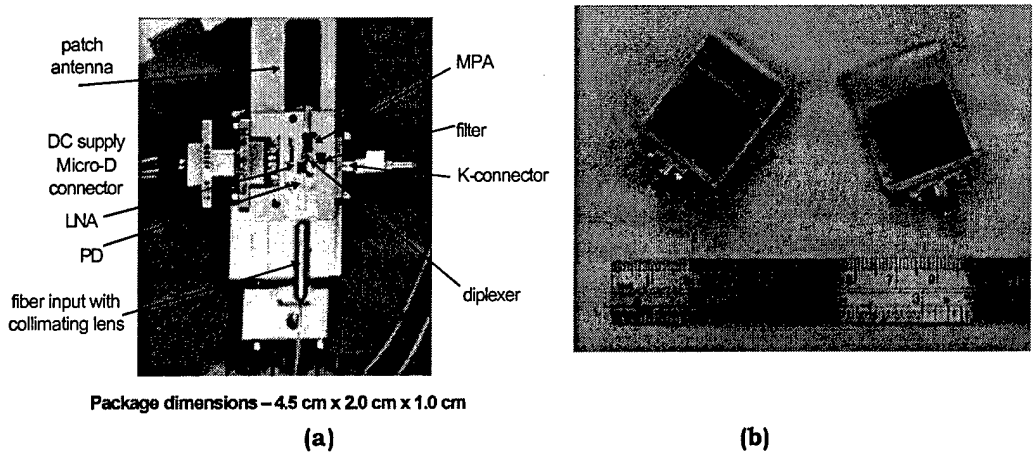


**Figure 1** Photographs of different integrated antenna/photonic device approaches: (a) hybrid integration; (b) direct integration

Of the previously developed procedures to create efficient antenna/photonic modules, there is a limiting commonality that each method tries to overcome. This is the fact that the O/E (or E/O) material is of a high dielectric constant value and because of this advanced electromagnetic techniques must be utilized to negate the impact of the

material on the overall efficiency. Despite these research endeavors, there are fundamental limits in terms of operation bandwidth that cannot be overcome due to this material composition. However, recently optical modulators based upon polymer materials have been developed and this material selection may be able to alleviate this issue. Effectively since the modulator can be developed on low dielectric constant material, the previously mentioned limitations can be overcome and the antennas can potentially be efficiently integrated with the photonic devices.

In this report we summarize the results to date on the integration of wideband printed antennas with polymer modulators conducted at Photonic Systems Inc (PSI) using the polymer modulators developed at the University of Southern California (USC). In Section II we give a brief introduction on the types of wideband printed antenna technologies and determine which is most suited to the application of integration. This decision was based on creating an antenna that can operate from 2 - 20 GHz. In this section we give a brief review of the chosen antenna and present the predicted and measured response of the developed antenna. In Section III we summarize the RF properties of the electrodes of the polymer modulators developed at USC. These are the modulators to be integrated with the antennas. In Section IV we present the results of integrating the modulator with the antenna and the measured losses associated with the integrated module. Finally, in Section V we present the performance of an optical link incorporating a polymer modulator and the developed wideband printed antennas.

## II Wideband Printed Antennas

Table I highlights the properties of common antennas that are relevant to the program here, namely, their bandwidth, how easily they can be integrated with a photonic device and how easily they can be developed into an array. From this table it is apparent that tapered slot radiators are best suited to give a solution that is both wideband and can easily be integrated with a modulator. Basic dipole and patch antennas do not satisfy the wideband bandwidth requirement and waveguide based antennas cannot be readily integrated with photonic devices. Spiral and log periodic antennas can provide wideband solutions, however their overall size results in an inefficient radiating solution if incorporated into an array.

| Antenna type | Bandwidth (fractional) | Can be integrated with modulator? | Can be used in an array? |
|---|---|---|---|
| **Dipole** | 1.2:1 | Yes | Yes |
| **Microstrip patch** | 1.1:1 | Yes | Yes |

| | | | |
|---|---|---|---|
| **Waveguide** | 1.3:1 | No | Yes |
| **Spiral and log periodic** | 10:1 | Yes | No |
| **Tapered slot** | >4:1 | Yes | Yes |

**Table I** Comparison of wideband antenna solutions

As the tapered slot appears to be the best solution, we then set about designing this radiator such that it can meet the bandwidth requirements as well as be integrated with a polymer modulator. It is also imperative that the antenna be as small as possible such that it is compliant with the requirement that an array of these radiators can be readily formed. To design the radiator we used a full-wave electromagnetic analysis tool. The software is based on the Finite Element Method and takes into consideration the finite edges of the copper cladded substrate used to develop the antenna.

The design methodology for the antenna utilized here was as follows. Firstly, the antenna was designed independent of the modulator. Then a transition was created that can match the transmission medium of the output of the modulator (in this case coplanar waveguide, CPW) to the input of the antenna (slot line). The entire antenna (including the transition) was then integrated and simulated. Finally we experimentally verified the predicted response of the antenna.

Figure 2 shows a schematic of the designed tapered slot without a transition to CPW. As can be seen from this figure, the taper profile is a piece wise linear taper that approximates an exponential profile. This was done to ease the manufacturing requirements for the fabrication of the antenna. The substrate used in the design process was *RT/Duroid 5870* with a height of 1.58 mm and a dielectric constant ($?_r$) of 2.33. The overall size of the antenna was 70 mm x 70 mm x 1.58 mm.

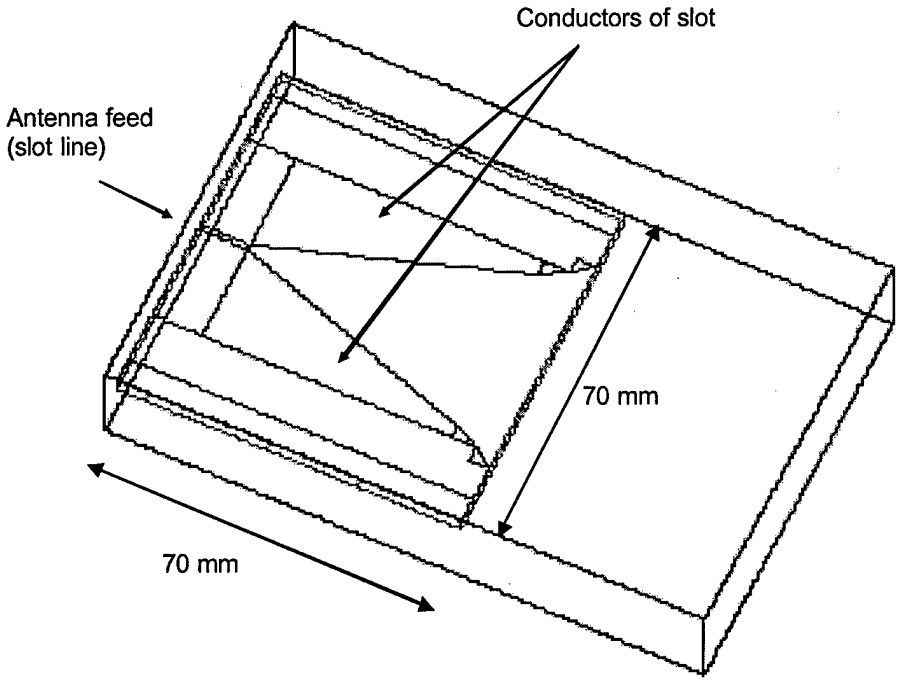


**Figure 2** Schematic of tapered slot antenna

Figure 3a shows the return loss response of the designed tapered slot. As can be seen from this plot the antenna easily meets the bandwidth requirement. The radiation pattern of the antenna at 10 GHz is shown in Figure 3b.

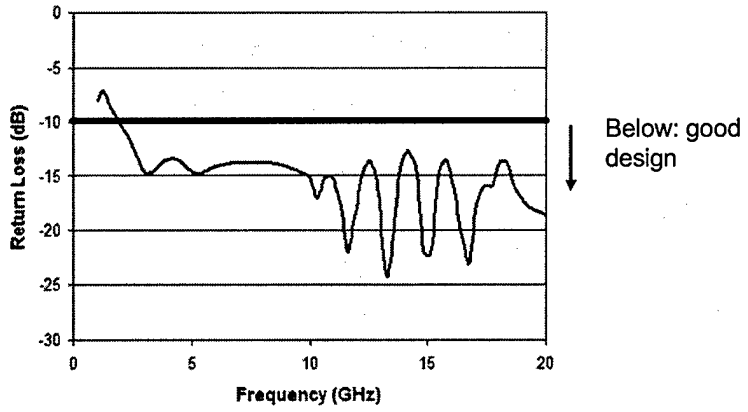


**(a)**

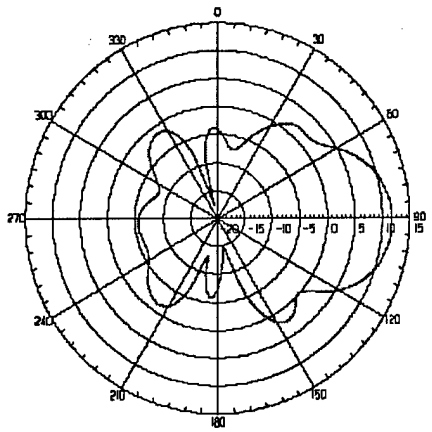


**(b)**

**Figure 3** Predicted performance of tapered slot antenna: **(a)** return loss; **(b)** radiation pattern at 10 GHz

There are several reported techniques that have been proposed to create a wideband transition from slot line to CPW. We decided to utilize one that is simple to fabricate and involves the minimum number of terminations. Figure 4 shows a schematic of the resulting transition. The circular structure is a wideband slot-line open circuit termination. The predicted characteristics of the transition are shown in Figure 5. Here the loss through the slot line to CPW transmission lines is approximately 3 dB and each termination is well matched.

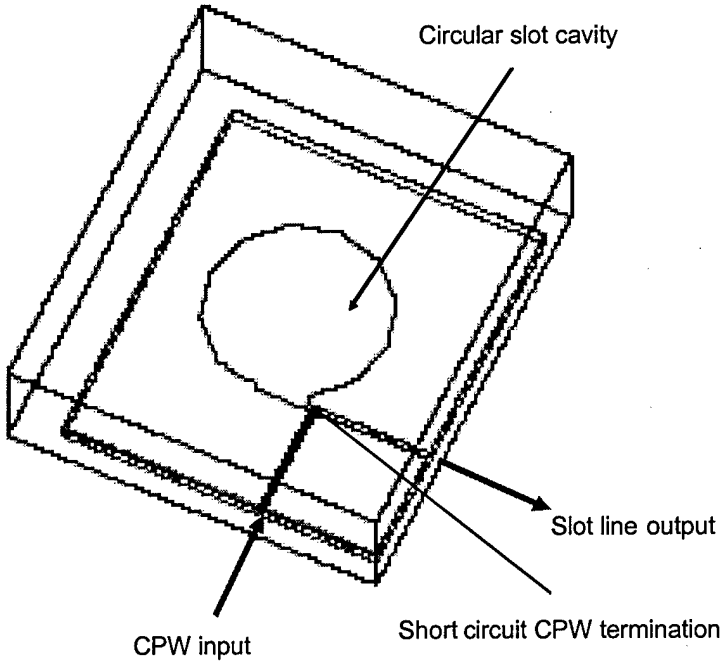


**Figure 4** Schematic of slot line to CPW transition

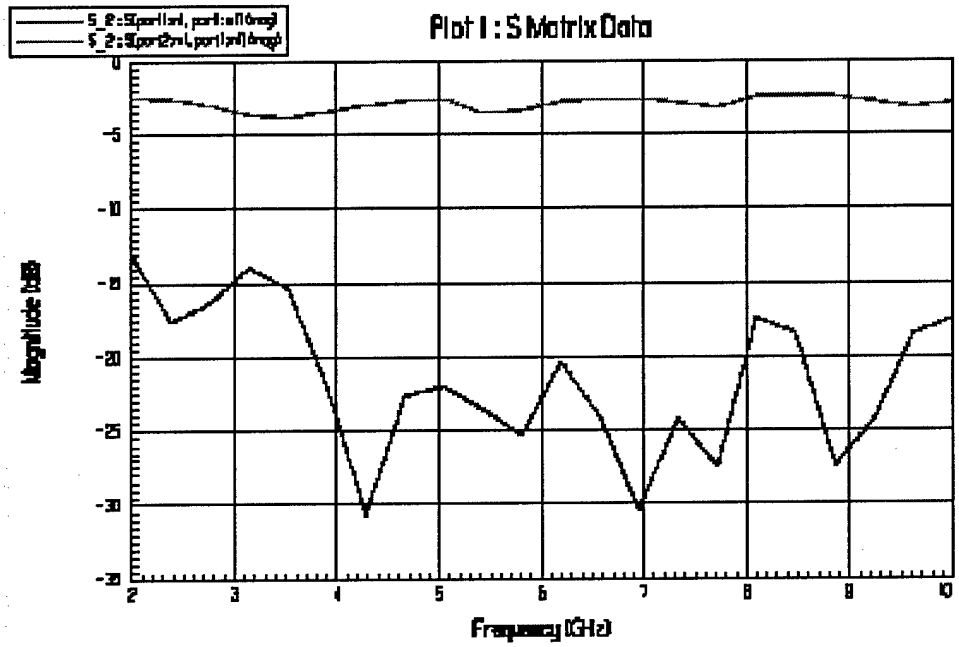


**Figure 5** Predicted performance of slot line to CPW transition

We then simulated the entire radiating structure (including the transition). Figure 6 shows a schematic of the resulting structure. The overall size (including the transition) is 115 mm x 90 mm. The predicted return loss and a typical radiation pattern of the antenna (at 10 GHz) are shown in Figure 7. As can be seen from these results, our predicted results show that our design meets the requirement of developing a wideband printed antenna that can easily be integrated with the CPW terminated polymer modulators.

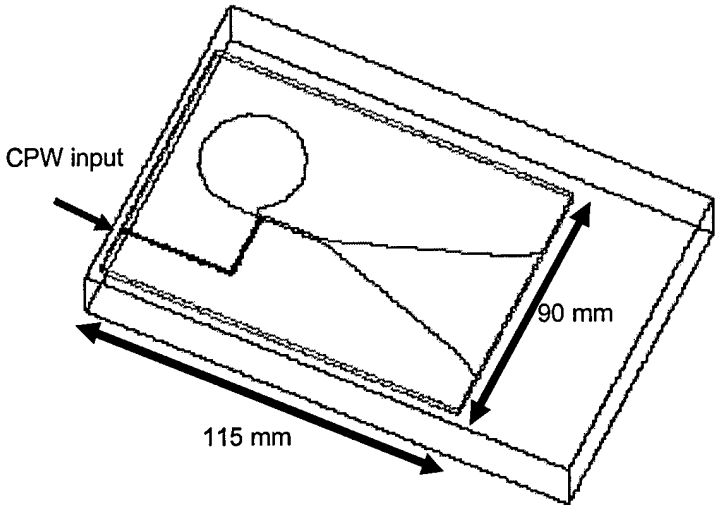

**Figure 6** Schematic of CPW fed tapered slot antenna

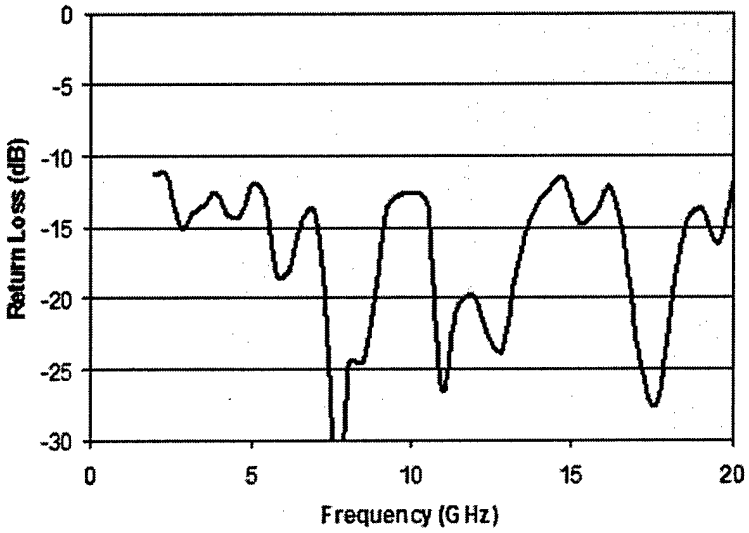


(a)

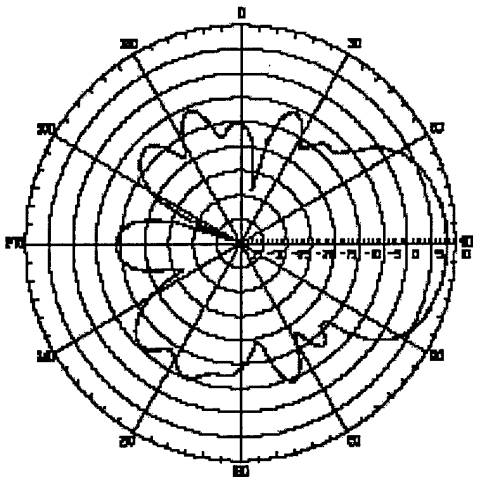

(b)

**Figure 7** Predicted results of CPW fed tapered slot antenna: **(a)** return loss; **(b)** radiation pattern at 10 GHz

The final phase of the antenna design was to experimentally verify the predicted results. Figure 8 shows a photograph of the etched tapered slot antenna. An SMA connector is adhered to the CPW feed using silver epoxy. The connector allowed us to measure the input impedance response of the antenna using a Vector Network Analyzer.

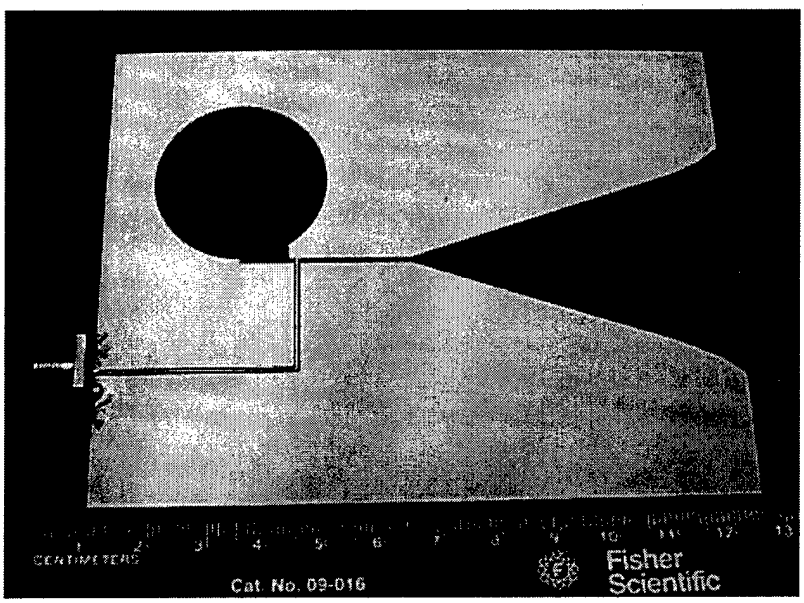


**Figure 8** Photograph of CPW fed tapered slot antenna

Figure 9 shows a comparison of the predicted and measured return loss of the developed CPW fed tapered slot antenna. As can be seen from these results, good agreement between theory and experiment was achieved. As the connector was not included in the numerical analysis of the printed antenna, we used time grating to minimize the finite reflections associated with this transition.

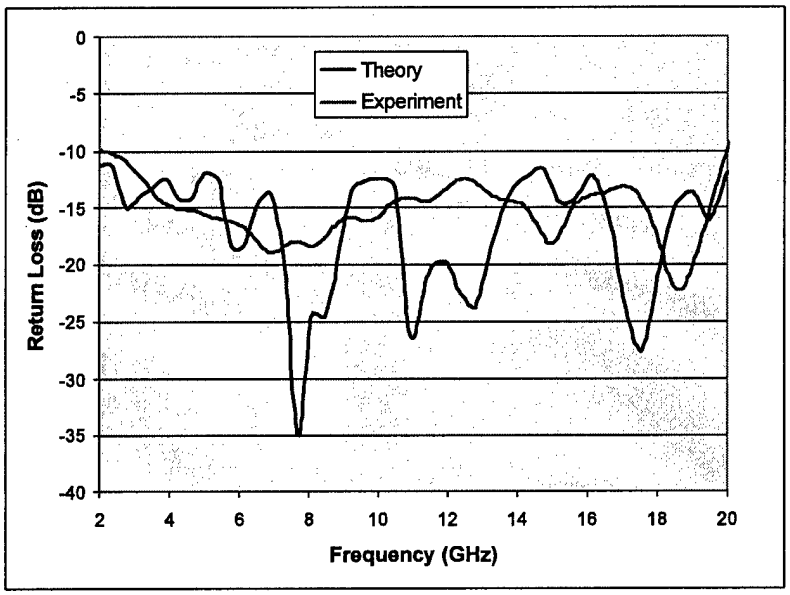

**Figure 9** Comparison of predicted and measured return loss of CPW fed tapered slot antenna

## III Measurement of RF properties of wideband Polymer Modulators

The next phase of this project was to measure the RF characteristics of the electrodes of the wideband polymer modulators. Here we measured the RF return loss and insertion loss of the electrode structure to ensure that it had minimal loss and also that we could match the antenna efficiently to the electrodes of the polymer device. Several electrode structures were considered and Figure 10 shows a photograph of the one chosen to be integrated with the printed radiator.

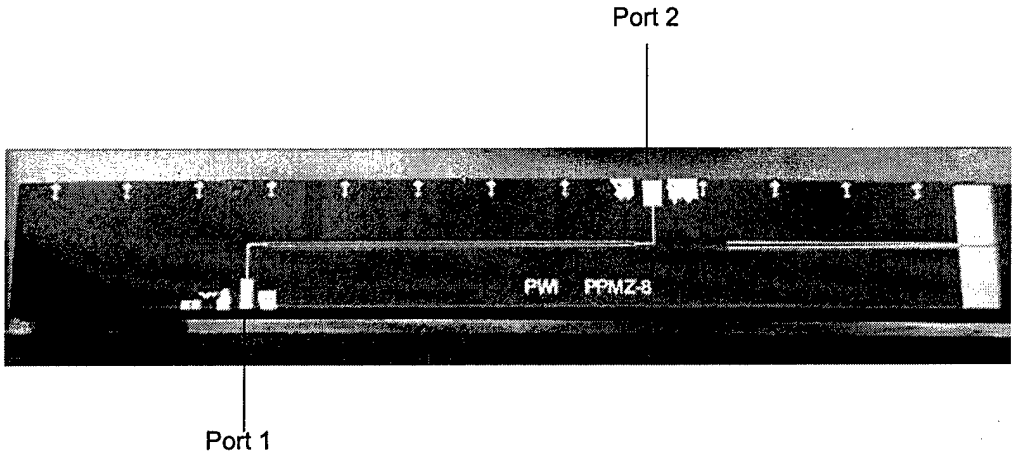


**Figure 10** Photograph of electrode structure of polymer modulator

Figure 11 shows the measured insertion loss and impedance response of the electrode structure. As can be seen from the measured S-parameters, the modulator has good insertion loss performance beyond 20 GHz and the impedance of the electrodes is approximately 40 ? up to this frequency.

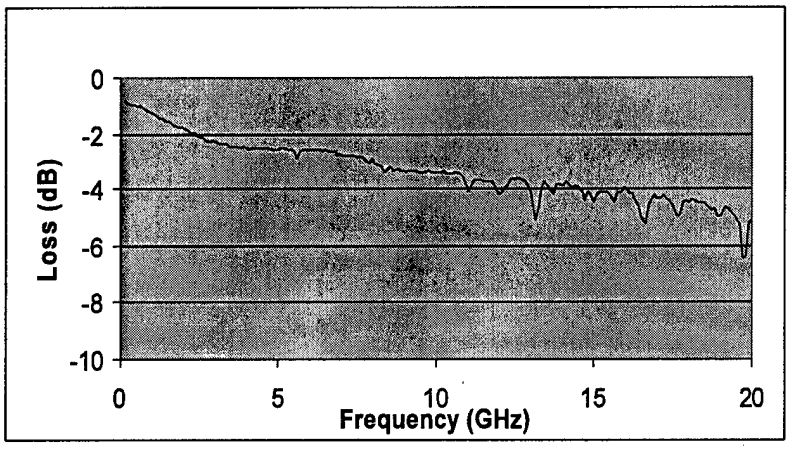

(a)

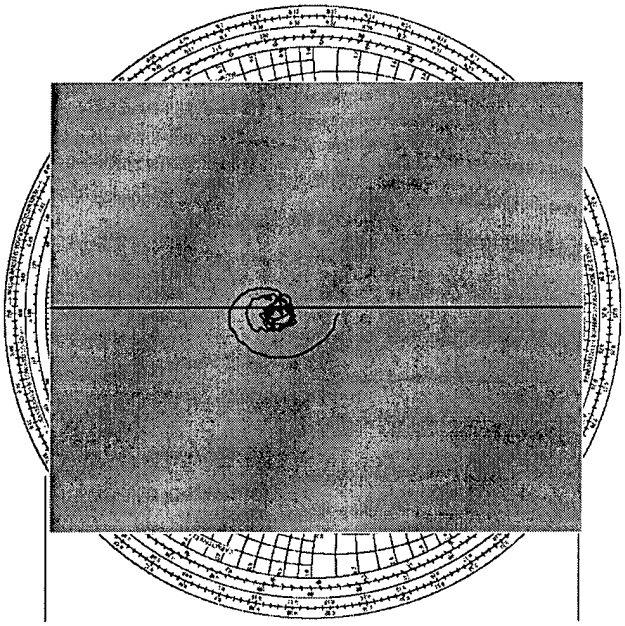

(b)

**Figure 11** Measured RF performance of electrodes of polymer modulator

## IV Integration Results

The next stage of the project involved the integration of the electrodes of the polymer modulator to the CPW fed tapered slot antenna. We used silver epoxy to interconnect the two devices and a small glass slide to support the polymer modulator. Figure 12 shows a photograph of the resulting structure.

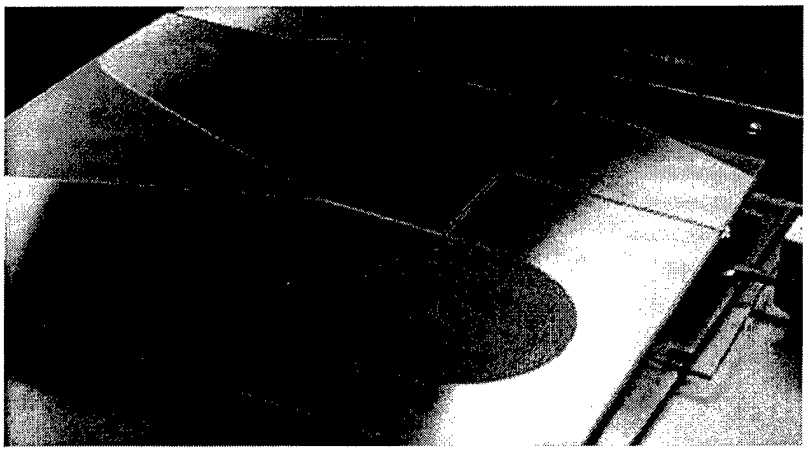

**Figure 12** Photograph of the integrated modulator tapered slot antenna

We then conducted an experiment to ascertain the performance of the integrated antenna/modulator. First we did a free space propagation measurement between 2 CPW fed tapered slot antennas from 1 - 20 GHz. We then substituted the integrated module into the experiment. Figure 13 shows both transmission measurements. The difference in power levels can be attributed to the insertion loss of the RF electrodes of the polymer modulator and also a mismatch created at the interconnection of the modulator and the antenna. Here a thin wire was used to connect the electrode of the modulator to the antenna and a slight gap existed between the structures. The results presented in Figure 13 are very good and shown that we can efficiently integrate a wideband printed antenna with a polymer modulator.

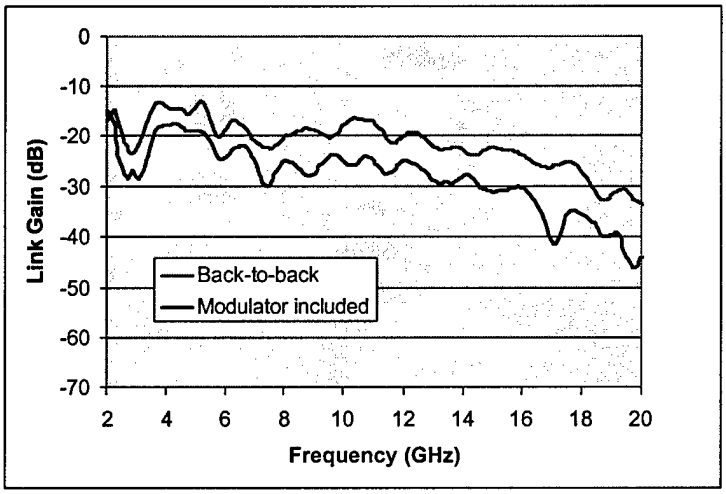


**Figure 13** Free space transmission measurements

## V Link Performance

The final aspect of this work was to develop a wideband RF over fiber link that incorporated both the newly developed polymer modulator and the CPW fed tapered slot antenna. The objective here was to demonstrate the capabilities of these developed components. Figure 14 shows a schematic of the experimental set-up used to investigate the link. As can be seen from this figure there are several components that normally would not be required for an RF optical link, however these were used to overcome some of the issues associated with the polymer modulator prototype. First of all the maximum input power the modulator could handle was 1 mW and so an optical attenuator was needed to lower the laser power level. This affects the achievable gain of the link. A polarization controller was also required as the input fiber into the prototype modulator was single mode fiber. As the modulator was a prototype, its insertion loss was relatively high and so an optical amplifier was used to boost the output signal. All of these issues will be resolved in later versions of the polymer modulator.

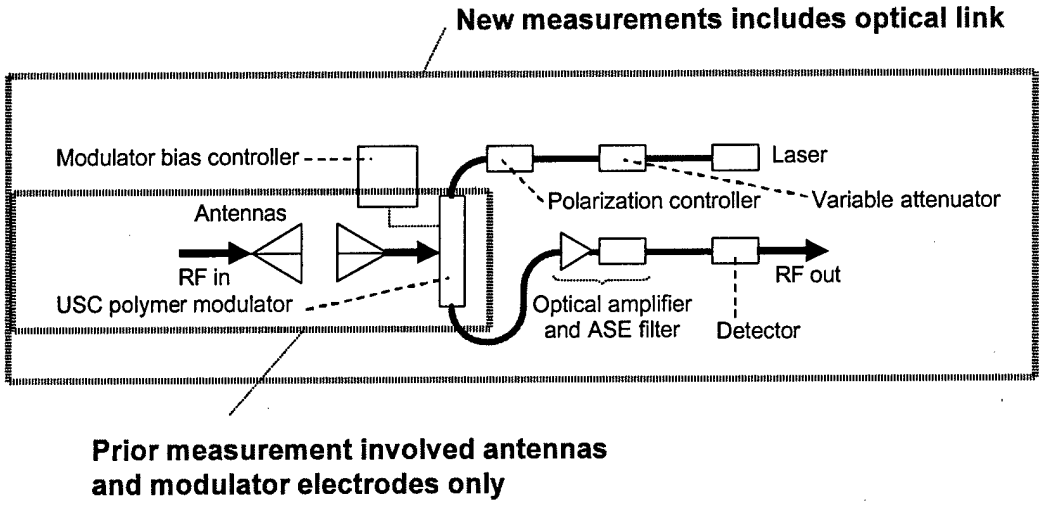


**Figure 14** Schematic of RF/optical link measurement

Figure 15 shows the measured responses of the RF/optical link from 1 - 20 GHz. Also shown in this plot are the predicted results. Very good agreement can be seen between experiment and theory.

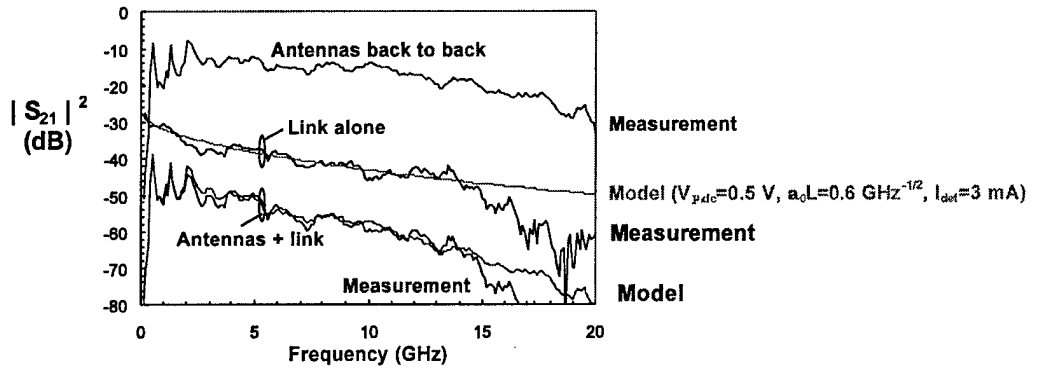


**Figure 15** RF/optical link performance: measured and predicted

## VI Conclusions

In this part we the project we investigated several aspects required for the successful, efficient integration of a polymer modulator with a wideband printed antenna for radar applications. In particular, we created an antenna capable of operating efficiently over the entire bandwidth of the modulator. Included in this work was the design of an efficient transition from the slot line of the tapered slot radiator to the CPW electrode of the modulator input. We also experimentally investigated how the modulator and antenna can be integrated and conducted RF optical link budget evaluations of the proposed modules.

## References

[1] R. B. Waterhouse, Microstrip Patch Antennas: A Designer's Guide, Kluwer, Boston, 2003.

[2] G. H. Smith, R. B. Waterhouse, A. Nirmalathas, D. Novak, C. Lim, and O. Sevimli, "A broadband integrated photonic-antenna interface for multiservice millimeter-wave fiber-wireless applications," MWP 2001, Long Beach California, pp. 173 – 176, Oct. 2001.

[3] W. S. T. Rowe and R. B. Waterhouse, "Efficient wideband printed antennas on Lithium Niobate for OEICs", *IEEE Transactions on Antennas & Propagation*, Vol. 51, pp. 1413 – 1415, June 2003.